General Disclaimer

One or more of the Following Statements may affect this Document

- This document has been reproduced from the best copy furnished by the organizational source. It is being released in the interest of making available as much information as possible.

- This document may contain data, which exceeds the sheet parameters. It was furnished in this condition by the organizational source and is the best copy available.

- This document may contain tone-on-tone or color graphs, charts and/or pictures, which have been reproduced in black and white.

- This document is paginated as submitted by the original source.

- Portions of this document are not fully legible due to the historical nature of some of the material. However, it is the best reproduction available from the original submission.

LMSC-D057194

UNSTEADY AERODYNAMIC FLOW FIELD ANALYSIS OF THE SPACE SHUTTLE CONFIGURATION

Part II: LAUNCH VEHICLE AEROELASTIC ANALYSIS

by

J. Peter Reding and Lars E. Ericsson

April 1976

Prepared Under Contract NAS 8-30652

for

National Aeronautics and Space Administration

Lockheed MISSILES and SPACE COMPANY, INC.

SUNNYVALE, CALIFORNIA

UNSTEADY AERODYNAMIC FLOW FIELD ANALYSIS OF THE SPACE SHUTTLE CONFIGURATION

Part II: LAUNCH VEHICLE AEROELASTIC ANALYSIS

by

J. Peter Reding and Lars E. Ericsson

April 1976

Prepared Under Contract NAS 8-30652

for

National Aeronautics and Space Administration

Lockheed Missiles & Space Company, Inc.
A Subsidiary of Lockheed Aircraft Corporation
Sunnyvale, California

ABSTRACT

An exploratory analysis has been made of the aeroelastic stability of the Space Shuttle Launch Configuration. The purpose of the analysis is to define critical flow phenomena with adverse aeroelastic effects and to develop simple analytic means of describing the time-dependent flow-interference effects so that they can be incorporated into a computer program to predict the aeroelastic stability of all free-free modes of the shuttle launch configuration.

Three critical flow phenomena have been identified:

1. Discontinuous jump of orbiter wing shock
2. Inlet flow between orbiter and booster
3. H.O. tank base flow

All involve highly nonlinear and often discontinuous aerodynamics which cause limit cycle oscillations of certain critical modes. Given the appropriate static data, the dynamic effects of the wing shock jump and the HO tank bulbous base effect can be analyzed using the developed quasi-steady techniques. However, further analytic and experimental efforts are required before the dynamic effects of the inlet flow phenomenon can be predicted for the shuttle launch configuration.

CONTENTS

ILLUSTRATIONS

ILLUSTRATIONS (Continued)

Figure

Section 1
INTRODUCTION

The present analysis is the first step toward the development of a technique for the prediction of the aeroelastic stability of the Space Shuttle Launch Vehicle. The quasi-steady approach is similar to that used so successfully for the Apollo-Saturn booster (Refs. 1-4). The technique was later mechanized (Ref. 5) and used routinely to predict the aerodynamic damping of the low frequency free-free bending modes of the various operational vehicles (Refs. 6-10), and was further extended to predict the gust penetration response (Ref. 11). The present analysis is specifically aimed at defining the critical, time-lag sensitive, flow phenomena and develop means of predicting their dynamic effects. Areas in need of further analytic and/or experimental investigations are pointed out.

Much valuable data are available in the literature (Refs. 12-15) on the rigid body dynamic stability of both orbiter and launch configurations. These data were invaluable to the present analysis. The approach taken was to first examine the rigid body dynamic stability data for the characteristic signature of a flow field time lag; i.e., opposite static and dynamic nonlinearities (statically stabilizing but dynamically undamping or vice-versa). Next static force, pressure, and flow visualization data were analyzed to determine the causes of these dynamic anomalies. The phenomena were then modeled using quasi-steady techniques to predict the dynamic measurements from static wind tunnel data.

Once a satisfactory match with the rigid body dynamic data was obtained, the analysis was applied to the elastic vehicle. For each phenomenon the aerodynamic damping was computed for modes where it had an undamping effect. This gave a representative indication of the seriousness of the various unsteady flow effects.

Because of the large number of modes that exist for the shuttle launch configuration only a few representative modes were analyzed. It cannot be known if these are worst case modes without analyzing all modes. However, a complete modal analysis will have to wait until the procedure is computerized for rapid calculation of a large number of cases.

Section 2
ORBITER UNSTEADY AERODYNAMICS

The orbiter wing is the major lift producing element of the launch configuration. Thus, it will dominate the elastic vehicle dynamics. It is natural, therefore, to first consider the unsteady aerodynamics of the orbiter alone without the complication of booster interference. Consequently, the analysis begins with the orbiter alone vehicle dynamics.

2.1 Orbiter Aerodynamics

Typical orbiter dynamic stability data (Refs. 12 and 13) are presented in Figure 1. The opposition between static and dynamic derivatives is indicative of a flow field time lag (Refs. 1, 2, and 16).* The sharp peaks in the stability derivatives suggest the possibility of highly nonlinear or discontinuous static stability characteristics (Refs. 17 and 18). Oilflow photographs (Ref. 19) indicate three flow types on the orbiter wing at transonic speeds (Fig. 2). At low angles of attack, the flow is essentially attached with a very small flow separation at the foot of the normal shock on the outboard wing (Fig. 2a). The forward shock appears to emanate from the forward edge of a corner separation at the wing fuselage juncture whereas the OMS pods fix the location of the aft shock** (Figures. 2a and 3a). At some intermediate angle of attack the corner separation jumps to the strake apex, and the forward shock also jumps forward quite near the wing leading edge. The wing shock induced pressure rise couples with the leading edge suction to produce a large adverse pressure gradient which causes a large region of flow separation to occur over the outer wing panel

*Stable $C_{mq} + C_{m\dot{\alpha}}$ excursions correlate with unstable $C_{m\alpha} - k^2 C_{m\dot{q}}$ excursions and vice versa.

**The OMS pods also effect the position of the forward shock via the corner separation as will be discussed later.

(Figs. 2b and 3b). Finally, at a high angle of attack, the shock moves all the way to the leading edge and the entire outer panel is stalled (Figs. 2c and 3c).

It is evident that the flow at the wing-fuselage juncture somehow alters the conventional two-dimensional shock-boundary layer interaction. Lock and Rodgers (Ref. 20) have described the mechanism whereby conditions at the wing fuselage juncture determine the position of the forward wing shock. The flow component normal to the leading edge is accelerated by expansion over the upper wing and, as a result, the resultant flow is turned toward the fuselage. The flow must eventually be turned parallel to the fuselage. This is accomplished via a compression that coalesces into a single shock; the forward wing shock. The similarity* to the orbiter wing flow is illustrated in Figure 4. It is the corner separation that furnishes the boundary condition that fixes the forward wing shock on the orbiter. When the separation jumps to the strake apex the boundary condition for the forward wing shock changes suddenly causing the shock to jump too.

The corner separation has a duality of character; (1) it acts as the boundary to which the leeside wing flow must adjust itself, (2) it is vented through a vortex which generates lift over the aft portion of the wing through vortex induced suction. Thus, it plays a fundamental role in producing all of the orbiter nonlinear stability characteristics illustrated in Figures 5, 6, and 7.

The discontinuous shock movement caused by the corner separation jump generates the jumps in C_N and C_m at $M = 1.2$. Although the density of the data points is generally insufficient to define the nonlinearities, the normal force data strongly suggest a highly nonlinear or discontinuous behavior between $\alpha = 8°$ and $\alpha = 10°$. A corresponding nonlinearity in $C_m(\alpha)$ is computed from the dynamic data (Refs. 12 and 13), as will be discussed later. Following the jump $C_{m\alpha}$ remains stabilizing and, as the vortex venting the corner separation grows with angle of attack, $C_{m\alpha}$ becomes more stabilizing while $C_{N\alpha}$ increases due to the vortex-induced suction over the aft wing (Refs. 21 and 22). Concurrently, C_A plateaus as the vortex

*Although the aft shocks have different origins.

suction opposes the usual reduction of C_A with α. Finally, at high α the wing stalls causing an unstable increment in C_m, a reduction in C_N and a decrease in C_A. These trends are generally pervasive despite changes in OMS pod configuration (Figs. 5, 6, and 7 and Refs. 23, 24, and 25, respectively). At M = 0.6, the data do not exhibit any discontinuity since no wing shock occurs at so low a Mach number. However, at $\alpha \approx 8°$ an increase in $C_{N\alpha}$ and a more stable $C_{m\alpha}$ occurs due to the effects of the wing-fuselage vortex. At high angles of attack, the stall nonlinearity is also evident.

The center of pressure of each of these nonlinear incremental variations in the static stability data have been computed; i.e.,

$$\Delta x_{cp} = \frac{C_{m\alpha} - C_{m\alpha o}}{C_{N\alpha} - C_{N\alpha o}} \qquad (1)$$

where the subscript o denotes the slope at $\alpha = 0$. The results are shown in Figure 8. These data indicate that the nonlinear effects occur on the aft wing panel for both static and dynamic measurements. Both static and dynamic nonlinearities correlate with the change in flow patterns from oilflow results (Fig. 9)*, further verifying that the wing flow is responsible for both static and dynamic nonlinearities.

The variation in the flow boundaries in Figure 9 are largely the result of variations in OMS pod configuration. Figure 10 shows that the wing flow patterns are sensitive to the OMS pod configuration (Refs. 19 and 26). The OMS pods directly effect the position of the aft wing shock and indirectly they also effect the position of the forward shock. The OMS pods create an adverse pressure gradient at the wing-fuselage juncture due to the OMS pod shock at high transonic speeds (Fig. 11a) and due to stagnation at the OMS induced downwash at lower speeds (Fig. 11b). This feeds upstream through the thick viscous layer at the wing-fuselage juncture, affecting the location of the corner separation and thus the forward wing shock. Unfortunately, the OMS pod configuration is the most changed configuration feature of the orbiter. It seems to be different for nearly every wind tunnel test. Of the static tests, the

*The oilflow photographs were taken at $\alpha = 5°$ increments; thus the 5° data bars in Figure 9.

OMS pod configuration in Ref. 23 is the one most like the pods of the dynamic model (Refs. 12 and 13).

2.2 Orbiter Rigid Body Dynamics

All evidence indicates that the strake-fuselage vortex dominates the orbiter wing loads for a large angle of attack range. Whether it is the discontinuous shock jump or the suction effect of the vortex, the nonlinear wing load is a function of the corner separation. For a first approximation it was assumed that the crossflow at the strake apex determines the boundary layer condition at the wing-fuselage juncture and thus the corner separation extent. When the separation occurs at the strake apex, the situation is similar to that for free-body vortices on slender bodies of revolution (Ref. 27). For the shuttle this means that the crossflow at the strake apex determines the position of the corner vortex relative to the aft wing, thus determining the aft wing lift. At high angles of attack the strake and main wing vortices combine into one vortex (Fig. 3c). This rolled up vortex is swept to the outboard wing panel where it bursts at stall. Thus, all the nonlinearities in the stability derivatives are determined by crossflow at the strake apex. In the dynamic case the induced load, the nonlinear increment, will lag the vehicle attitude due to the finite convection speed of the vortices (Ref. 28). That is, the induced pitching moment is a function of the angle of attack at the strake apex at an earlier time (Refs. 6 and 22);

$$\Delta^{i}C_{m} = \Delta^{i}C_{m\alpha}\,\alpha_{A}\,(t-\Delta t) \tag{2}$$

$$\Delta t = \frac{x_A - x_s}{\bar{U}} = c\,\frac{(\xi_A - \xi_s)}{\bar{U}}$$

where x_A is the apex station, x_s is the induced load station, and $\bar{U} = U$ is the convection speed of the vortex (Ref. 22). With the definitions in Fig. 12

$$\alpha = \alpha_0 + \theta - \frac{\dot{z}}{U}$$

and

$$\left.\begin{aligned} \alpha_A\,(t-\Delta t) &= \alpha_0 + \theta\,(t-\Delta t) - c\,\xi_A\,\frac{\dot\theta}{U}\,(t-\Delta t) \\ \theta\,(t-\Delta t) &= e^{-i\omega\Delta t}\theta\,(t) = \theta\,(t)\cos(\omega\Delta t) - i\theta\,(t)\sin(\omega\Delta t) \\ \dot\theta &= \omega\left[i\ \theta\ (t)\right] \end{aligned}\right\} \tag{4}$$

therefore

$$\theta\,(t-\Delta t) = \theta\,(t)\cos(\omega\Delta t) - \frac{\dot\theta(t)}{\omega}\sin(\omega\Delta t) \tag{5}$$

and

$$\dot\theta\,(t-\Delta t) = \dot\theta\,(t)\cos(\omega\Delta t) - \frac{\ddot\theta(t)}{\omega}\sin(\omega\Delta t) \tag{6}$$

The aerodynamic inertia ($\ddot\theta$) terms are negligible.

Combining equations (2), (3), (4) and (5) gives

$$\frac{\partial\,\Delta^i C_m}{\partial\left(\frac{\dot\theta c}{2U}\right)} = -2\ \Delta^i C_{m\alpha}\left[\frac{\sin(\omega\Delta t)}{\bar\omega} + \xi_A\cos(\omega\Delta t)\right] \tag{7}$$

where $\bar\omega = \frac{\omega c}{U}$

and

$$\Delta^i C_{m_\alpha} = C_{m_\alpha} - C_{m_{\alpha o}} \tag{8}$$

The induced damping derivative is added to the attached flow damping derivative for angles of attack where the strake-fuselage vortex occurs, i.e., for $\alpha \geq \alpha_v$

$$\frac{\partial C_m}{\partial\left(\frac{\dot\theta c}{2U}\right)} = \frac{\partial\Delta^i C_m}{\partial\left(\frac{\dot\theta c}{2U}\right)} + \frac{\partial C_{ma}}{\partial\left(\frac{\dot\theta c}{2U}\right)} \tag{9}$$

and for $\alpha < \alpha_v$

$$\frac{\partial C_m}{\partial\left(\frac{\dot{\theta} c}{2U}\right)} = \frac{\partial C_{ma}}{\partial\left(\frac{\dot{\theta} c}{2U}\right)} \tag{10}$$

where

$$\frac{\partial C_{ma}}{\partial\left(\frac{\dot{\theta} c}{2U}\right)} = 2\, C_{m_{\alpha o}} \left[\xi_T\right]^2 \tag{11}$$

ξ_T is the trailing edge of the equivalent orbiter slender delta wing (Refs. 21 and 22). Eqs. (9) and (10) can be used to estimate the orbiter damping as long as the induced pitching moment derivative is finite and constant; however, when the corner separation jumps, $\Delta^i C_{m\alpha} = \infty$. An equivalent static moment derivative can be defined by integrating the discontinuous moment curve over the oscillation amplitude (Ref. 29).

$$C_{\bar{m}_\theta} = \frac{1}{\Delta\theta^2} \int_{-\Delta\theta}^{\Delta\theta} C_m \, d\theta = C_{m_{\alpha 0}} + \frac{\Delta C_m}{\Delta\theta}\left[1 - \frac{\alpha_D - \alpha_o}{\Delta\theta}\right] \tag{12}$$

provided that $\alpha_o \leq \alpha_D \leq \alpha_o + \Delta\theta$ and $-\alpha_D < \alpha_o - \Delta\theta$

where ΔC_m is the moment discontinuity and $\Delta\theta$ the oscillation amplitude; likewise, the equivalent damping derivative is defined by integrating over the cycle (Ref. 29).

$$\frac{\partial C_{\bar{m}}}{\partial\left(\frac{\dot{\theta} c}{2U}\right)} = \frac{2}{\pi \Delta\theta \ \bar{\omega}} \int_{\psi_o}^{\psi_o + 2\pi} C_m(\psi) \cos\psi \, d\psi \tag{13}$$

where $\psi = \omega t$ and $2\pi = \omega T$; T is the period of oscillation (Fig. 13).

This gives (following the method of Ref. 29);

$$\frac{\partial C_{\bar{m}}}{\partial\left(\frac{\dot{\theta} c}{2U}\right)} = \frac{\partial C_{ma}}{\partial\left(\frac{\dot{\theta} c}{2U}\right)} - \frac{4\Delta C_m}{\pi\bar{\omega}\Delta\theta}\left[\sin\beta \cos\psi\right] \tag{14}$$

where $$\psi = \sin^{-1}\left[\frac{\alpha_D - \alpha_o}{\Delta\theta}\cos\beta\right]$$

and $$\tan\beta = 2\left[\frac{\sin\omega\Delta t}{\bar{\omega}} + \xi_A\cos\omega\Delta t\right]\frac{\omega c}{2U}$$

The magnitude of the moment discontinuity (ΔC_m) was estimated from the spikes in $C_{m\alpha} - k^2 C_{mq}$. from the dynamic test data (e.g., at $\alpha = 2$ and 8 degrees in Figures 1a and 1b, respectively) using Eq. (12) (where $\Delta\theta = 1°$).* These values were then substituted into Eq. (14) to obtain the damping spikes. The rest of the damping curve was computed using the static data of Ref. 23 since that OMS configuration best approximates the OMS configuration of the dynamic model. In Figure 13 the results of these estimates are compared to the Langley damping measurements (Ref. 12). The agreement is gratifying since it verifies the flow model. Actually, in the stall region the time lag should probably be somewhat longer than that used in the present analysis as indicated by dynamic experiments (Ref. 30). This would give better agreement with the experimental damping values. However, stall occurs at too high an angle of attack to be of concern for the launch configuration. Thus, it is unnecessary to pursue the stall analysis further.

*This is how the discontinuities in Figures 5-7 were obtained.

Section 3
LAUNCH CONFIGURATION DYNAMICS

Armed with a satisfactory model of the unsteady aerodynamics of the orbiter wing one can now set out to analyze the dynamics of the launch configuration.

3.1 Launch Configuration Aerodynamics

Rigid body pitch damping data for the launch configuration (Ref. 14) also exhibit the characteristic signature of a flow field time lag (Figs. 14 and 15). At $M = 1.2$ the large undamping peak at $\alpha = 2.2°$ suggest a pitching moment discontinuity. Shadowgraph photographs indicate a region of flow separation on the HO tank due to the detached orbiter bow shock (Fig. 16).

Pressure distribution data (Ref. 31) indicate how this separation responds to angle of attack (Fig. 17). Crossflow over the HO tank nose forward of separation results in a thickening of the leeside boundary layer which in turn causes a forward movement of the separation point. The separation point location is a nonlinear function of angle of attack (Fig. 18).* The terminal normal shock standing between the orbiter and HO tank exhibits a nonlinear aft movement that correlates with the forward movement of the orbiter bow shock (Figs. 17 and 18). Likewise, the static pressures aft of the shock on both the HO tank top and the orbiter bottom also exhibit a nonlinearity that correlates with the shock movement. Thus, the entire flow field is coupled. This is the first indication that the flow between the stages is analogous to inlet flow (Ref. 32).

*In fairing the shock position curve the discontinuity has been positioned at $\alpha = 2.2°$ to correspond with the dynamic data.

The position of the normal shock between the stages is determined by the mass flow that can be accommodated by the more or less two-dimensional channel between the stages from the strake apex aft to the HO tank base. Any excess mass flow must be spilled laterally upstream of the strake. The flow upstream of the orbiter bow shock is aligned axially and spilling begins aft of the shock. The spilling is a function of the pressure distribution over the top of the HO tank. When the pressures are high a relatively large amount of mass flow is forced out laterally. However, when the pressure drops, as it does under the orbiter nose, the outflow decreases. When the orbiter bow shock is in its aft position the area of high pressure is reduced and less mass flow is spilled. In order to get rid of the excess mass flow the normal shock between stages moves forward, giving an additional high pressure region forward of the strakes, which spills the excess mass flow. Of course this does not happen instantaneously; a considerable time lag is involved. The effect of an angle of attack change must first be convected downstream to the orbiter bow shock before the separation point can move. The excess mass flow must then be convected into the "inlet", and the "inlet" must fill before the normal shock is forced forward to the new equilibrium position. This filling time can be quite long, especially when one considers the considerable area for venting between the stages.

3.2 Launch Configuration Rigid Body Dynamics

It is impossible to estimate the time lag theoretically. However, the combination of static pressure data, dynamic stability data, and quasi-steady theory supplies the tools necessary for estimating the time-lag. If both the static and dynamic effects of the discontinuity are known, Eq. (14) can be used to estimate the time lag, Δt. This has been done for $M = 1.2$ using an iterative procedure. The jump increment was first taken in reference to the attached flow level* to obtain a first estimate of the time lag. Then the plateau level for $\alpha \geq -2^\circ$, on both sides of the undamping peak (Fig. 15), was computed. The jump was then incremented from the plateau and a second time lag determined. After just two iterations the results shown in Figures 19

*The attached flow damping was estimated using first order momentum theory (Ref. 33) for a slender body. Static force measurements for the launch configuration were used to improve accuracy.

and 20 were obtained. The jump loads and the effect of the continuous shock movement were estimated by integrating the pressure data of Ref. 31 (Figs. 21 and 22 respectively).

The very long time lag (the vehicle travels 26.2 orbiter lengths during Δt) is not unreasonable for inlet flows (Ref. 32). The good agreement with the Langley results is strong evidence that the flow model is valid.

The inlet flow effect is not restricted to $M = 1.2$ but occurs over the Mach number range $0.9 \leq M \leq 1.4$ (Figs. 23-25). However, at $M = 0.9$ the discontinuity in the shock position is not present since the shock stands so close to the shoulder. This explains why no undamping peak appears in the $M = 0.9$ dynamic data (Fig. 14) although the plateau is present. The plateau is well predicted from the static induced derivatives (from the integrated pressure data of Ref. 31) with $\omega\Delta t = 60°$ (Fig. 26). Evidence of the strake-fuselage vortex effect is also present in the $M = 0.9$ data. The damping spike is well predicted if one assumes that the wing shock jumps at $\alpha = 4.5°$, rather than at $\alpha = 2.2°$ as it did for the orbiter alone. Evidently the HO tank and SRM's reduce the crossflow at the strake apex so the corner separation jump does not occur until $\alpha = 4.5°$. Using the same ratio $\alpha_{booster}/\alpha_{orbiter}$ of 2.0 the shock jump will not occur until $\alpha = 16°$ at $M = 1.2$ explaining why it was not observed in the booster damping data for $\alpha \leq 6°$ (Fig. 15 and Ref. 13).

Another, simpler flow model was postulated earlier in the study. It was assumed that the induced loads did not involve an inlet-like flow. Rather, the orbiter bow shock was treated as a simple terminal normal shock with only boundary layer convection and accelerated flow time lag (Refs. 17 and 18). It was necessary to assume a large (.7 degree) amplitude hysteresis loop in order to predict the undamping peak at $M = 1.2$ (Fig. 27). However, the plateau could not be accounted for, using the continuous separation movement, because the time lag was too small. Although it is not conclusive, this certainly provides further evidence to support the inlet flow model.

Yaw damping data for the launch configuration with and without SRM's (Ref. 14) exhibit nonlinear damping characteristics (Fig. 28) that are indicative of bulbous base undamping with possible sting interference effects (Refs. 34 and 35). A good approximation to the yaw damping results is obtained for the configuration with SRM's off by simply carpet plotting the base increment from Ref. 36 to account for base radius and proximity to the sting flare*,and adding the increment to the first order attached flow damping estimate (Fig. 29). Of course the agreement for the configuration with SRM's on is not nearly as good since the SRM's certainly alter the base flow.

Unfortunately, further experimental data are needed in order to separate the sting interference effect from the free wake bulbous base effect. Actually, three induced loads affect the dynamics of bulbous bases (Fig. 30). Forebody crossflow effects thicken the leeside boundary layer. This causes the leeside separation point on the base to move forward, creating a separation asymmetry that causes a statically destabilizing base load (Fig. 30a). This load is aerodynamically undamping due to the time lag associated with convecting the boundary layer from nose to base. The free wake effect results from the pressure gradient across the inclined wake at $\alpha \neq 0$ that eventually turns it in the streamwise direction. The pressure gradient causes higher windward side wake neck pressures that are convected forward to the separation point, causing a separation asymmetry on the base that produces a statically stabilizing aerodynamically undamping base load (Fig. 30b). Finally, the asymmetric sting flare causes a wake flipping effect,that results in yet another statically stabilizing, undamping, base load (Fig. 30c).

*The sting configuration used in obtaining the data in Refs. 14 and 36 is identical.

Section 4
AEROELASTIC STABILITY

The equation of motion of the elastic vehicle describing single degree-of-freedom bending oscillations can be written (Refs. 1 and 2).

$$\tilde{m}\left\{q(t) + 2\omega\left[\zeta - \frac{B}{2\omega U}(D_s + D_a)\right]\dot{q}(t) + \omega^2\left[1 - \frac{B}{\omega^2}(K_s + K_a)\right]q(t)\right\} = P(t) \tag{15}$$

where $P(t)$ is the buffeting force input.

One requirement for stability is that the coefficient of $\dot{q}(t)$ cannot be negative. i.e.

$$\zeta - \frac{B}{2\omega U}(D_s + D_a) \geq 0 \tag{16}$$

where D_s and D_a are the aerodynamic damping derivatives in separated and attached flow respectively (a negative coefficient is damping). ζ is the structural damping as a fraction of critical and $-\frac{B}{2\omega U} = -\frac{\rho U S}{4\omega\tilde{m}}$ puts the aerodynamic damping into the same form as the structural damping. For a discontinuous aerodynamic load the damping is obtained by integrating over one cycle similar to what was done for the rigid body damping (Refs. 17 and 18).

$$D_s = \frac{\phi(\xi_s)\, c}{\pi \Delta q\, \bar{\omega}} \int_{\beta}^{2\pi+\beta} C_N(\psi) \cos\psi \, d\psi \tag{17}$$

For the discontinuous wing load illustrated in Figure 12 the instantaneous angle of attack is

$$\alpha_i = \alpha_o + \theta - \frac{\dot{z}}{U} \tag{18}$$

The jump effect is the result of conditions at the strake apex at the time $t-\Delta t$. Therefore

$$\alpha_i = \alpha_o + \theta_A\,(t-\Delta t) - \frac{\dot{z}_A\,(t-\Delta t)}{U} \tag{19}$$

with the elastic body coordinate system (Fig. 31).

$$\begin{aligned} \theta_A\,(t-\Delta t) &= \phi'\,(\xi_A)\,q\,(t-\Delta t) \\ z_A\,(t-\Delta t) &= \phi(\xi_A)\,\dot{q}\,(t-\Delta t) \end{aligned} \tag{20}$$

and

$$\begin{aligned} q\,(t-\Delta t) &= q\cos\,(\omega\Delta t) - \frac{\dot{q}}{\omega}\sin\,(\omega\Delta t) \\ \dot{q}\,(t-\Delta t) &= \dot{q}\cos\,(\omega\Delta t) - \frac{\ddot{q}}{\omega}\sin\,(\omega\Delta t) \end{aligned} \tag{21}$$

where $q = \Delta q \sin \omega t$

Therefore,

$$\begin{aligned} \alpha_i = \alpha_o + \phi'\,(\xi_A)\,\Delta q \;\Big[&\sin\,(\omega t)\cos\,(\omega\Delta t) \\ &- \cos(\omega t)\sin(\omega\Delta t)\Big] - \frac{\phi(\xi_A)}{U}\Delta q\omega\Big[\cos(\omega t) \\ &\cos(\omega\Delta t) + \omega\,\sin(\omega t)\sin(\omega\Delta t)\Big] \end{aligned} \tag{22}$$

or

$$\begin{aligned} \alpha_i = \alpha_o + \sec\,\beta\;\Big[&\phi'(\xi_A)\cos\,\omega\Delta t \\ &- \phi(\xi_A)\,\frac{\omega}{U}\,\sin\,\omega\Delta t)\Big]\cdot\Delta q\,\sin\,\,(\psi-\beta) \end{aligned} \tag{23}$$

where $\psi = \omega t$

and

$$\beta = \tan^{-1}\left\{\frac{\phi'(\xi_A)\sin\omega\Delta t + \phi(\xi_A)\frac{\omega}{U}\cos\omega\Delta t}{\phi'(\xi_A)\cos\omega\Delta t - \phi(\xi_A)\frac{\omega}{U}\sin\omega\Delta t}\right\} \tag{24}$$

Thus, for the discontinuity that occurs at $\alpha_i = \alpha_D$

$$\psi_D = \sin^{-1}\left\{\frac{(\alpha_D - \alpha_o)\cos\beta}{\Delta q\left[\phi'(\xi_A)\cos\omega\Delta t - \phi(\xi_A)\frac{\omega}{U}\sin\omega\Delta t\right]}\right\} \tag{25}$$

The effect of the discontinuous orbiter wing load is found from applying Eq. (17) to the characteristics of Figure 12, i.e.

$$\bar{D}_s = \frac{\phi(\xi_s)\,c}{\pi\Delta q\,\omega}\left\{\int_{\beta}^{\beta+\psi_D} C_{N_1}(\psi)\cos\psi d\psi + \int_{\beta+\psi_D}^{\pi+\beta-\psi_D} C_{N_2}(\psi)\cos\psi d\psi + \int_{\pi+\beta-\psi_D}^{2\pi+\beta} C_{N_1}(\psi)\cos\psi d\psi\right\} \tag{25}$$

where

$$C_{N_1} = C_{N_{\alpha 1}}\left[\alpha_o + \phi'(\xi_A)\Delta q\sin\psi\right];\ \text{for}\ \alpha_i \le \alpha_D$$

$$C_{N_2} = C_{N_{\alpha 2}}\left[\alpha_o + \phi'(\xi_s)\Delta q\sin\psi\right] + \Delta C_N\frac{\alpha_i}{|\alpha_i|};\ \text{for}\ \alpha_i > \alpha_D \tag{26}$$

Integrating gives

$$\bar{D}_s = -\frac{2\phi(\xi_s)\,c}{\pi\Delta q\bar{\omega}}\Delta C_N\sin\beta\cos\psi_D \tag{27}$$

The aerodynamic damping is

$$\zeta_a = -\frac{\rho US}{4\omega\tilde{m}} \left[\bar{D}_s + D_a\right] \tag{28}$$

where

$$D_a = -C_{N_\alpha} \left[\phi(\xi_T)\right]^2 \tag{29}$$

$C_{N\alpha}$ is the attached flow normal force derivative of the boost configuration.

Some discussion of the limits of applicability of the quasi-steady theory is appropriate before presenting results of the analysis. A simple description of the limits of the technique is given in Ref. 37 and Figure 32. It shows clearly that as long as the wavelength (λ) of the interference effect is large relative to the characteristic dimension (c) of the effected body element the quasi-steady technique is valid (i.e., when $c/\lambda \leq .25$). When the characteristic length approaches the 1/2 wave length it is possible to get an upwash over the leading edge of the submerged body simultaneously with a downwash at the tail. Thus, the single lumped tail load approximation is no longer valid. Refining the approximation through the representation of the load distribution by several lumped loads is not the answer since the leading edge will alter the upwash (or wave shape) over downstream portions of the body. Thus, the applicability of the quasi-steady technique becomes questionable. Of course the limit is not rigid and the applicability of the results will gradually deteriorate as c/λ exceeds 0.25.

From Eq. (27) one can see that when the vehicle is describing infinitesimal amplitude oscillations (Δq) at $\alpha_o = \alpha_D$ with $\psi_D = 0$ the induced damping $\bar{D}_s \to \infty$. As the oscillation amplitude increases D_s becomes finite. Limit cycle oscillations will occur for modes such as the one shown in Figure 33 when the coefficient of $\dot{q}(t)$ in Eq. (15) is zero. If the structural damping is zero, $\zeta = 0$ in Eqs. (16) and (28), limit cycle oscillations occur at $\bar{D}_s + D_a = 0$ (Fig. 34). A more realistic value of the structural damping is $\zeta = .01$; therefore, a limit cycle oscillation occurs where

$$\zeta = .01 = -\frac{\rho US}{4\omega\tilde{m}} \left[D_a + \bar{D}_s\right] \tag{30}$$

For the mode in Figure 33 limit cycle oscillations will occur for $M = 0.9$ and 1.2 (Fig. 34). This limit cycle value is conservative in the sense that it may not have time to develop, but is unconservative in the sense that no coupling with other modes has been included. To determine exactly how large the maximum limit cycle will be requires a more complete modal analysis.

Rather late in the study the work of Chipman and Rauch (Ref. 38) became available to the authors. Although their analysis revealed no aeroelastic instabilities at $\alpha = 0$ the location of the node line of the first torsional mode gives reason for concern in regard to the wing shock jump at $\alpha > 0$. Figure 35 shows the nodal line superimposed on $M = 1.2$ oil flow photographs. The shock moves forward of the node line with increasing angle of attack. The negative shock induced load will be aerodynamically undamping when it is forward of the node (Fig. 26). The statically destabilizing jump load was damping for rigid body oscillations. However, the sign of the jump moment about the wing node is reversed and it will therefore cause undamping. It appears that the shock jump will be undamping at $M = 0.9$ as well (Fig. 36). Time did not permit an analysis of the torsional mode; however it appears that at the very least limit cycle oscillations are possible in the range $.9 \leq M \leq 1.2$, when the wing shock jump occurs.

The OMS pod configuration has a strong influence on the wing shock position. Little or no flow separation occurs forward of the streamlined OMS pods; however, a very large separation occurs forward of the blunt OMS pods (Fig. 10). That the OMS pods affect the position of the wing shock is shown in Figure 37. Evidently the vortices that vent the separation on the orbiter canopy energize the boundary layer on the top of the orbiter causing the separation to shrink and the orbiter wing shocks to move back with the separation. This is an effect of the blunt OMS pods that has not been analyzed as yet; however, the effect should be significant as it involves the orbiter wing load and the convection time of the vortices from canopy to OMS pod, which is nearly the same as the strake vortex lag. It appears that this effect can be analyzed with the same techniques used for the strake-fuselage effect on the wing shock.

The inlet like flow between orbiter and booster involves massive discontinuous loads which will certainly result in limit cycle oscillations for critical modes. Figure 38 illustrates such a critical mode. Damping results are presented in Figure 39. Because of the very long time lag associated with the inlet flow even small errors in the time lag result in a large variation in the phase angle. Thus, for a 2.5% uncertainty in the time lag (which is easily within the accuracy of the time lag estimates) the damping results cover the gambit from strongly damped to undamped with a limit cycle oscillation (Fig. 39). Unstable regions also repeat every 1/2 cycle (Fig. 40). The quasi-steady results are highly questionable in this case even though the technique is valid from the standpoint of interaction length to wave length ratios ($c/\lambda \leq .25$). The applicability is suspect because the "inlet walls" make 20 pulsations during the long time lag. Nevertheless, the possible implication of the inlet flow (possible structural failure) is serious enough to warrant further investigation to assure structural integrity.*

The bulbous base effect has been analyzed for the mode shown in Figure 41. Unfortunately the free wake effect cannot be separated from the sting interference effect with the information currently available. Thus, the wake interference increment was simply taken from the data of Figure 30 and applied directly to the booster mode (Figure 41) to obtain the results in Figure 42. Of course, the bulbous base effect could be very sensitive to exhaust plumes, which have not been accounted for in these estimates. Judging by the amount of aerodynamic undamping predicted without plumes it seems prudent to investigate the bulbous base effect including the effect of exhaust plumes. This can be accomplished with currently available quasi-steady techniques given the static sting deflection derivative and plume increments.

*The effects of exhaust plumes and control deflections must be included in such a study.

Section 5
CONCLUSIONS

An exploratory analysis of the space shuttle boost configuration has revealed three unsteady flow phenomena that cause aerodynamic undamping of certain critical free-free bending modes;

1. Wing shock jump
2. Inlet flow between stages
3. HO tank base flow

Of the three effects items one and two involve discontinuous aerodynamics that result in limit cycle oscillations of certain critical free-free bending modes. The wing shock jump affects both booster bending modes and orbiter wing torsional modes.

Limit-cycle oscillations threaten the structural integrity in two ways; either by outright overstressing the structure due to large modal deflections or via fatigue. Fatigue is a much more serious problem for the reusable shuttle orbiter than it was for the single flight Apollo-Saturn vehicles. Since limit cycle oscillations will certainly affect fatigue life a complete modal analysis is recommended to define the limit cycles for all critical modes.

Given the proper static aerodynamic data the wing shock jump and the HO tank base flow effects can be predicted using present quasi-steady techniques. However, the quasi-steady technique runs into accuracy problems for the inlet flow problem. Furthermore, the evidence supporting the inlet flow model is somewhat tenuous. It is, therefore, recommended that the inlet flow be thoroughly investigated experimentally. Perhaps the most useful information could be obtained from a fluctuating pressure test of the flow between the stages. Coherence results could show conclusively the coupling of the inlet flow and would furnish accurate convection speed measurements that could be applied to the computation of the modal damping of the flight vehicle via quasi-steady techniques.

All three unsteady flow phenomena will be sensitve to Reynolds number since they all involve flow separation. Since the quasi-steady theory relies on static wind tunnel data, which is usually obtained for Reynolds numbers two or three orders of magnitude below the flight value, the effect of Reynolds number on the induced loads must be understood to allow extrapolations to full scale. It is recommended that the effects of Reynolds number on these critical unsteady flow mechanisms be investigated to determine proper scaling techniques. Additionally a means of simulating the full scale Reynolds number in a subscale wind tunnel test by boundary layer trip design, location, etc. needs to be developed to properly simulate the full scale unsteady flow effects.

REFERENCES

1. Ericsson, L.E., and Reding, J.P., "Report on Saturn I - Apollo Unsteady Aerodynamics," LMSC/A650215, Feb. 1964.

2. Ericsson, L.E., and Reding, J.P., "Analysis of Flow Separation Effects on the Dynamics of a Large Space Booster," J. Spacecraft and Rockets, Vol. 2, No. 4, July-Aug. 1965, pp. 481-490.

3. Rainey, A.G., "Progress the Launch Vehicle Buffeting Problem," J. Spacecraft and Rockets, Vol. 2, No. 3, May-June 1965, pp. 289-299.

4. Hanson, P.W., and Dogget, R.V., Jr., "Wind Tunnel Measurements of Aerodynamic Damping Derivatives of a Launch Vehicle Vibrating in Free-Free Bending Modes at Mach Numbers from 0.7 to 2.87 and Comparison with Theory," NASA TN D-1391, 1962.

5. Davis, N.L., "Computer Program for Quasi-Steady Aeroelastic Analysis," LMSC M-37-67-3, Dec. 1967.

6. Ericsson, L.E., and Reding, J.P., "Technical Summary Report, Aeroelastic Characteristics of Saturn IB and Saturn V Launch Vehicles," LMSC Report M-37-67-5, Dec. 1967.

7. Davis, N.L., "The Aeroelastic Characteristics of the Saturn V Launch Vehicle SA-505," LMSC Report M-30-69-2A, April 1969.

8. Davis, N.L., "The Aeroelastic Characteristics of the Saturn V Launch Vehicles, SA-506 and an Updated SA-505, LMSC Report N-3C-69-2B, June 1969.

9. Davis, N.L., "The Aeroelastic Characteristics of the Saturn V Launch Vehicle SA-507 for Launch Dates of 14 November and 16 November 1969," LMSC Report N-36-69-2C (2nd Addendum to LMSC N-3C-69-2A), Oct. 1969.

10. Davis, N.L., "The Aeroelastic Characteristics of the Saturn V Launch Vehicle SA-508 for April 1970 Launch Date," LMSC Report M-3C-69-2D, (3rd Addendum to LMSC Report N-36-29-2A) Oct 1969.

11. Ericsson, L.E., Reding, J.P., and Guenther, R.A., "Gust Penetration Loads and Elastic Vehicle Response for Saturn V Vehicles," LMSC Report N-3C-70-2, July 1970.

12. Boyden, R.P., and Freeman, D.C., "Subsonic and Transonic Dynamic Stability Derivatives of a Modified 089B Shuttle Orbiter," NASA TMX 72631, Dec. 1974.

13. Freeman, D.C., Jr. and Boyden, R.C. and Davenport, E.E., "Supersonic Dynamic Stability Derivatives of a Modified 089B Shuttle Orbiter," NASA TMX 72630, Oct. 1974.

14. Freeman, D.C., Jr. and Boyden, R.P., "Subsonic and Transonic Dynamic Stability Results (R1 Space Shuttle Launch Vehicle)," NASA LA 44.

15. Freeman, D.C., Jr. and Boyden R.P., "Supersonic Dynamic Stability Results (R1 Space Shuttle Vehicle), NASA LA 43A and B.

16. Ericsson, L.E., and Reding, J.P., "Dynamics of Separated Flow over Blunt Bodies," Technical Summary Report, LMSC 2-80-65-1, Dec. 1965.

17. Ericsson, L.E., "Aeroelastic Instability Caused by Slender Payloads," J. Spacecraft and Rockets, Vol. 6, No. 12, pp. 1404-1409, Dec. 1969.

18. Ericsson, L.E., French, N.J. and Guenther, R.A., "The Aeroelastic Characteristics of the Saturn 1B Launch Vehicle with Biconic Payload Shroud," LMSC Report M-37-67-1, July 1967.

19. Nichols, M.E., "Results of Investigation on the 0.004-scale model 74-0 of the Configuration 4 (Modified) Space Shuttle Orbiter in the NASA/MSFC 14 by 14 inch, Trisonic Wind Tunnel (0A131)," NASA CR 141, 521, March 1975.

20. Lock, R.C., and Rodgers, E.W.E., "Aerodynamic Design of Swept Wings and Bodies for Transonic Speeds," Proceedings of 2nd International Congress of Aeronautical Sciences, 1960.

21. Ericsson, L.E., and Reding, J.P., "Unsteady Aerodynamic Analysis of Space Shuttle Vehicles, Part II; Steady and Unsteady Aerodynamics of Sharp-Edged Delta Wings," LMSC-D352326, Part II, August 1973.

22. Ericsson, L.E., and Reding, J.P., "Unsteady Aerodynamic Flow Field Analysis of the Space Shuttle Configuration," Part I: Orbiter Aerodynamics, LMSC/D057194, Part I, April 1976.

23. Allen, E.C., and Lindhall, R.H., "Investigation in the MSFC TWT to verify the Static Stability and Control Effectiveness of the 0.004-Scale Model (74-0) of the Shuttle 5 Orbiter (0A-108)," NASA CR 141, 537, June 1975.

24. Sparks, V.H., and Moser, M.M., Jr., "Wind Tunnel Tests of an 0.015-Scale Configuration 140 A1B Space Shuttle Orbiter Model (67-0) in the NASA LRC 8-foot TPT to Obtain Transonic Aerodynamic Force Data (0A-106)," NASA CR 134, 426, June 1975.

25. Hardin, R.B., and Burrows, R.R., "Wind Tunnel Tests of an 0.019-Scale Space Shuttle Integrated Vehicle in the NASA Ames 8 x 7-foot Unitary Wind Tunnel (1A-120)," NASA CR 141,518, April 1975.

26. Reding, J.P., and Ericsson, L.E., "Unsteady Aerodynamic Analysis of Space Shuttle Vehicles, Part III; Booster Interference Effects," LMSC-D352326, Part II, Aug. 1973.

27. Schiff, L.B., and Tobak, M., "Results from a New Wind-Tunnel Apparatus for Studying Coning and Spinning Motions on Bodies of Revolution," AIAA Journal, Vol. 8, No. 11, Nov 1970, pp 1953-1957.

28. Lamborne, N.C., Bryer, D.W., and Maybery, J.F.M., "A Preliminary Note on the Behavior of the Leading-Edge vortices of a Delta Wing Following a Sudden Change in Incidence," NPL Aero Note 1006, March 13, 1962.

29. Ericsson, L.E., "Separated Flow Effects on the Static and Dynamic Stability of Blunt Nosed Cylinder Flare Bodies," LMSC/667991, Contract NAS 8-5558, Dec. 1965.

30. Sawyer, S.A., Private Communication, University of Salford, England, May 1972.

31. Gillins, R.L., "Airloads Investigation of an 0.030-Scale Model of the Space Shuttle Launch Vehicle 140A1B Launch Configuration (Model 47-OTS) in the ARC 11-foot Unitary Plan Wind Tunnel for Mach Range 0.6 to 1.4 (1A14A)," NASA CR 134, 445, March 1975.

32. Dailey, C.E., "Supersonic Diffuser Stability," J. of the Aeronautical Sciences, Vol. 22, No. 11 Nov. 1955, pp. 733-749.

33. Bisplinghoff, R.L., Ashley, H. and Halfman, R.L., "Aeroelasticity," Addison-Wesley, Cambridge, Mass., 1955 pp. 418-419.

34. Reding, J.P., and Ericsson, L.E., "Dynamic Support Interference," J. Spacecraft and Rockets, Vol. 9, No. 7, July 1972, pp. 547-553.

35. Ericsson, L.E., and Reding, J.P., "Aerodynamic Effects of Bulbous Bases," NASA CR 1339, Aug. 1969.

36. Adcock, J.B., "Some Experimental Relations Between the Static and Dynamic Stability Characteristics of Sting-Mounted Cones with Bulbous Bases," Transactions of the 3rd Technical Workshop on Dynamic Stability Problems, Paper 5, Vol. II, 4-7 Nov. 1968, NASA Ames Research Center, Moffett Field, Calif.

37. Reding, J.P., and Ericsson, L.E., "Unsteady Aerodynamic Flow Field Analysis of the Space Shuttle Configuration, Part IV, 747/Orbiter Aeroelastic Stability, LMSC-D057194, Contract NAS 8-30652, March 1976.

38. Chipman, R.R., and Rauch, F.J., "Analytical and Experimental Study of the Effects of Wing-Body Aerodynamic Interference on Space Shuttle Subsonic Flutter," NASA CR-2488, Jan. 1975.

Appendix A
NOMENCLATURE

b	wing span
c	reference length; mean aerodynamic chord
D	damping derivative of elastic body, Eq. (15)
K	spring constant, Eq. (15)
M	free stream Mach number
m	pitching moment; coefficient, $C_m = m/(\rho U^2\ 2)/Sc$
N	normal force; coefficient, $C_N = N/(\rho U^2\ 2)/S$
n	yawing moment; coefficient, $C_n = n/(\rho U^2\ 2)/Sb$
P(t)	buffeting force
q	pitch rate
q(t)	normalized coordinate
r	yaw rate
S	reference area; wing area
t	time
U	free stream velocity
x	horizontal coordinate; (Fig. 12)
z	vertical coordinate; (Fig. 12)
α	angle of attack
α_o	trim angle of attack
β	yaw angle

Δ	increment
ξ	dimensionless horizontal coordinate, $\xi = x/c$
ζ	structural damping, fraction of critical
ζ_a	aerodynamic damping, fraction of critical
θ	pitch angle (Fig. 12)
λ	wavelength
ρ	free stream density
ϕ	normalized modal deflection (Fig. 31)
ϕ'	normalized modal slope (Fig. 31)
ψ	ωt
ω, $\overline{\omega}$	circular frequency, $\overline{\omega} = \omega c/U$

Subscripts

A	strake apex
a	attached flow
D	discontinuity
S	separated flow
T	denotes trailing edge of equivalent delta wing
V	vortex formation
o	denotes zero angle of attack

Superscripts

i	induced e.g. $\Delta^i C_N$ = separation induced normal force
'	$\partial/\partial x$
·	d/dt
··	d^2/dt^2

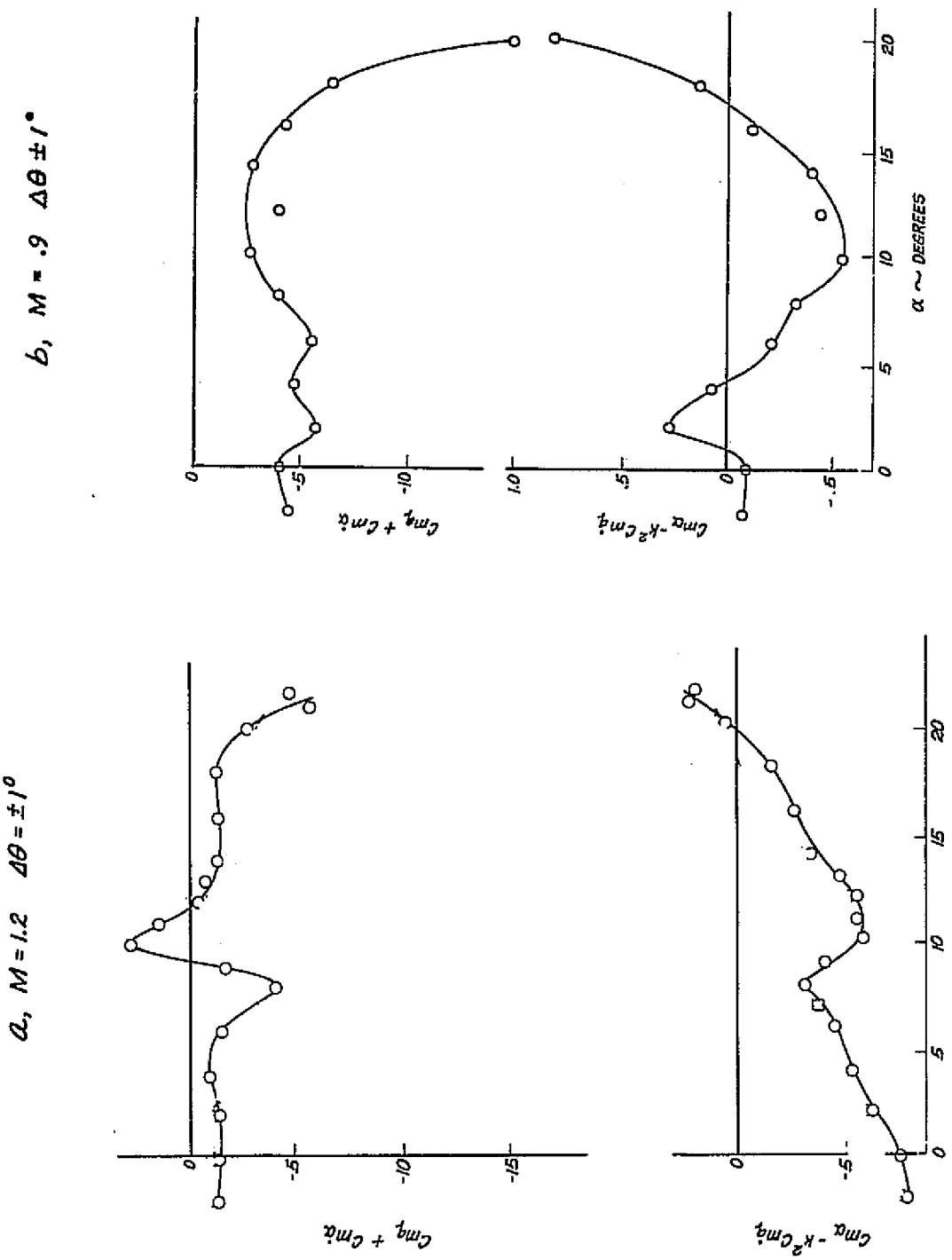

Figure 1 Typical Orbiter Dynamic Stability Data

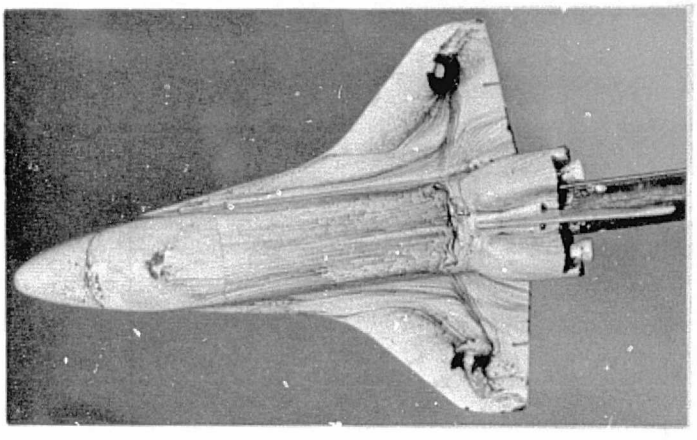

a) $\alpha = 5°$

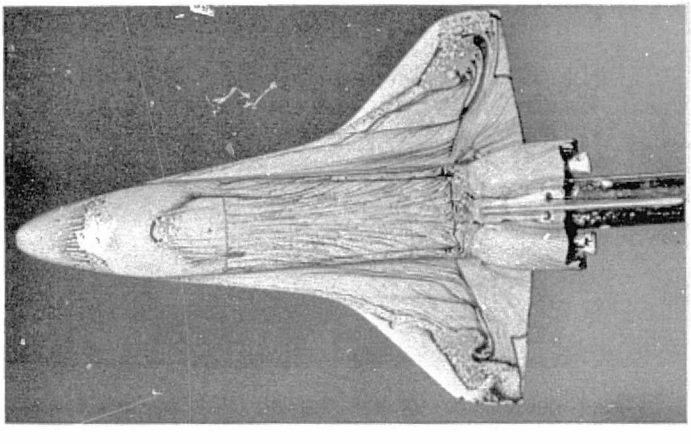

b) $\alpha = 10°$

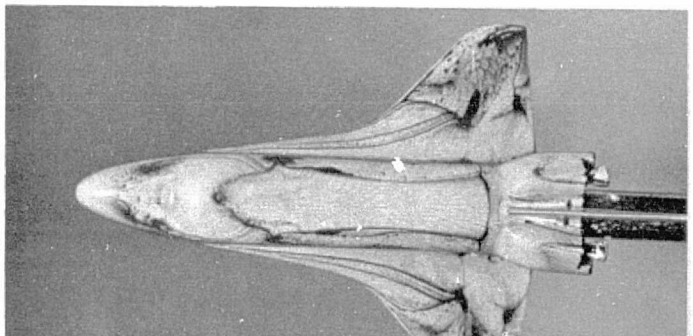

c) $\alpha = 25°$

Figure 2 Orbiter Leeside Flow Patterns

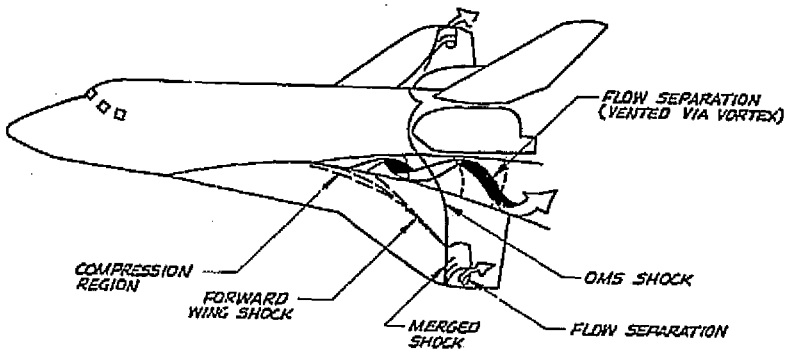

a.) LOW α

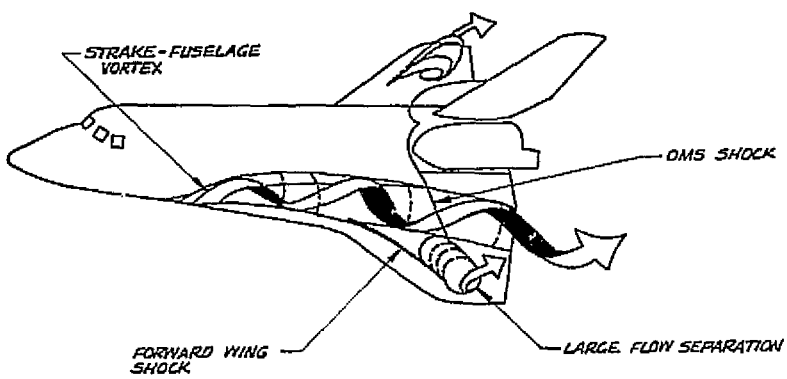

b) INTERMEDIATE α

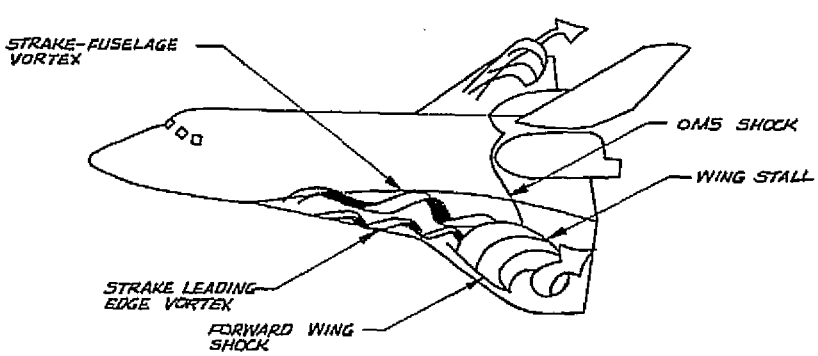

C) HIGH α

Figure 3 Sketches of Orbiter Wing Flow

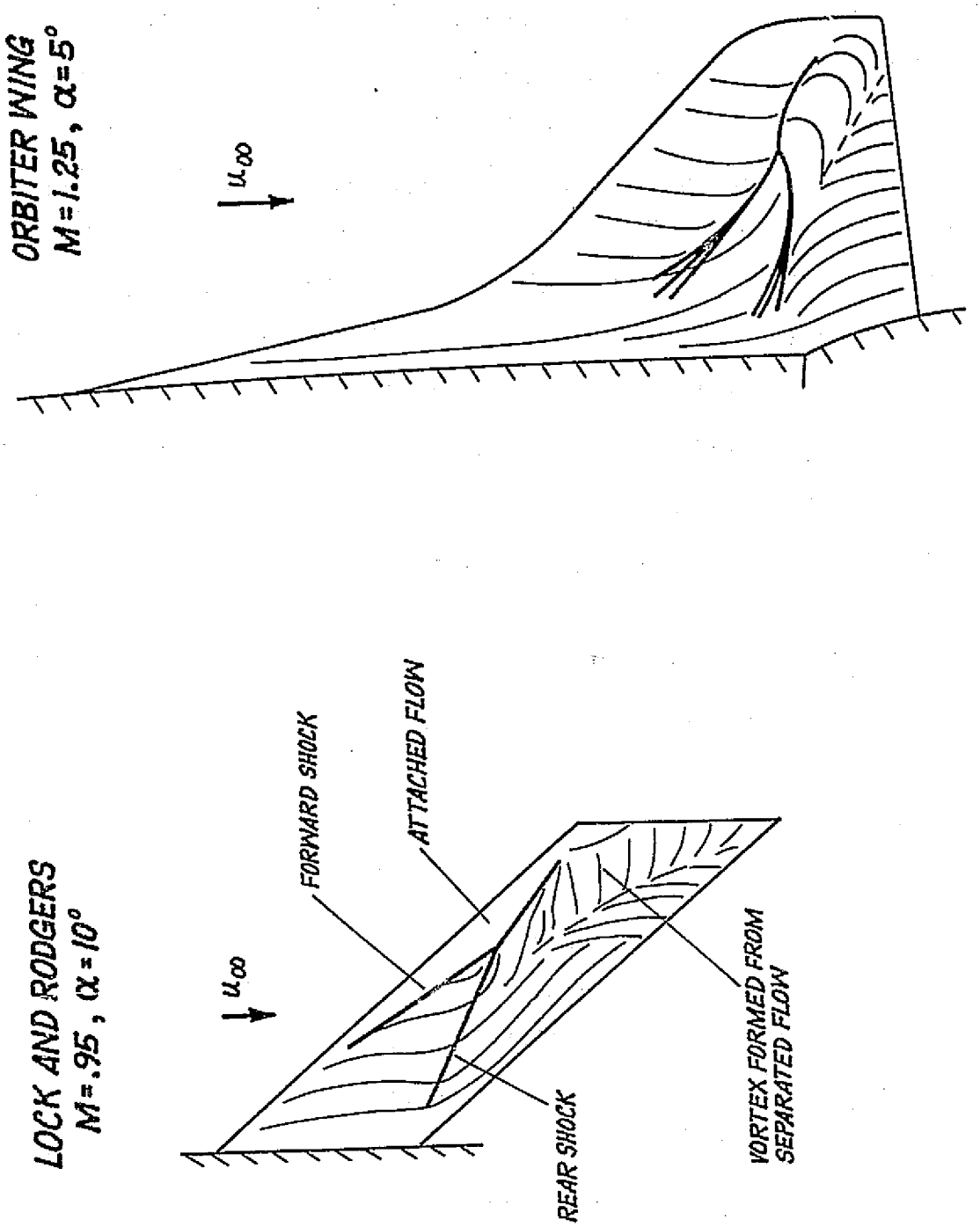

Figure 4 Comparison of Leeside Wing Flows

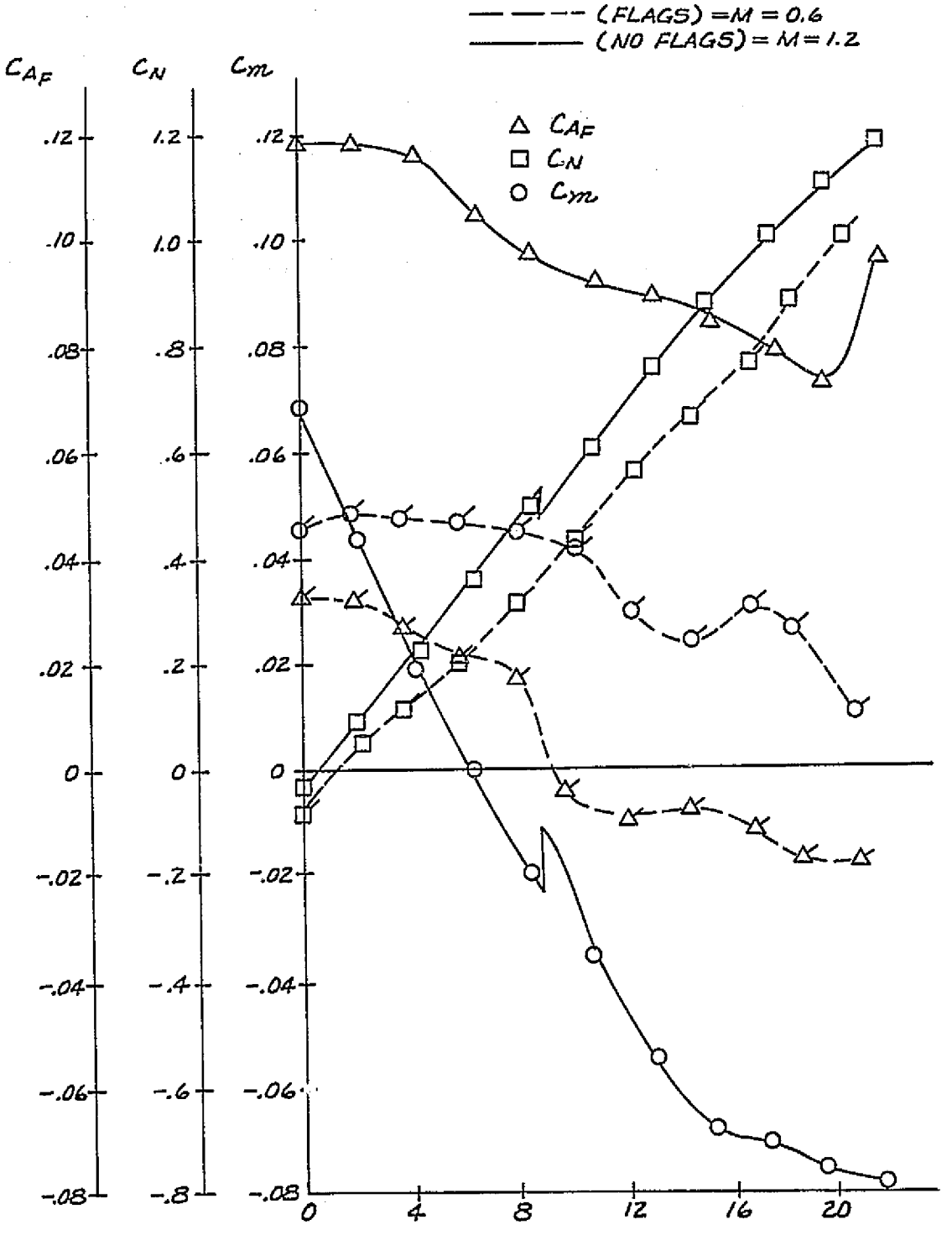

Figure 5 Typical Static Data (Ref. 23)

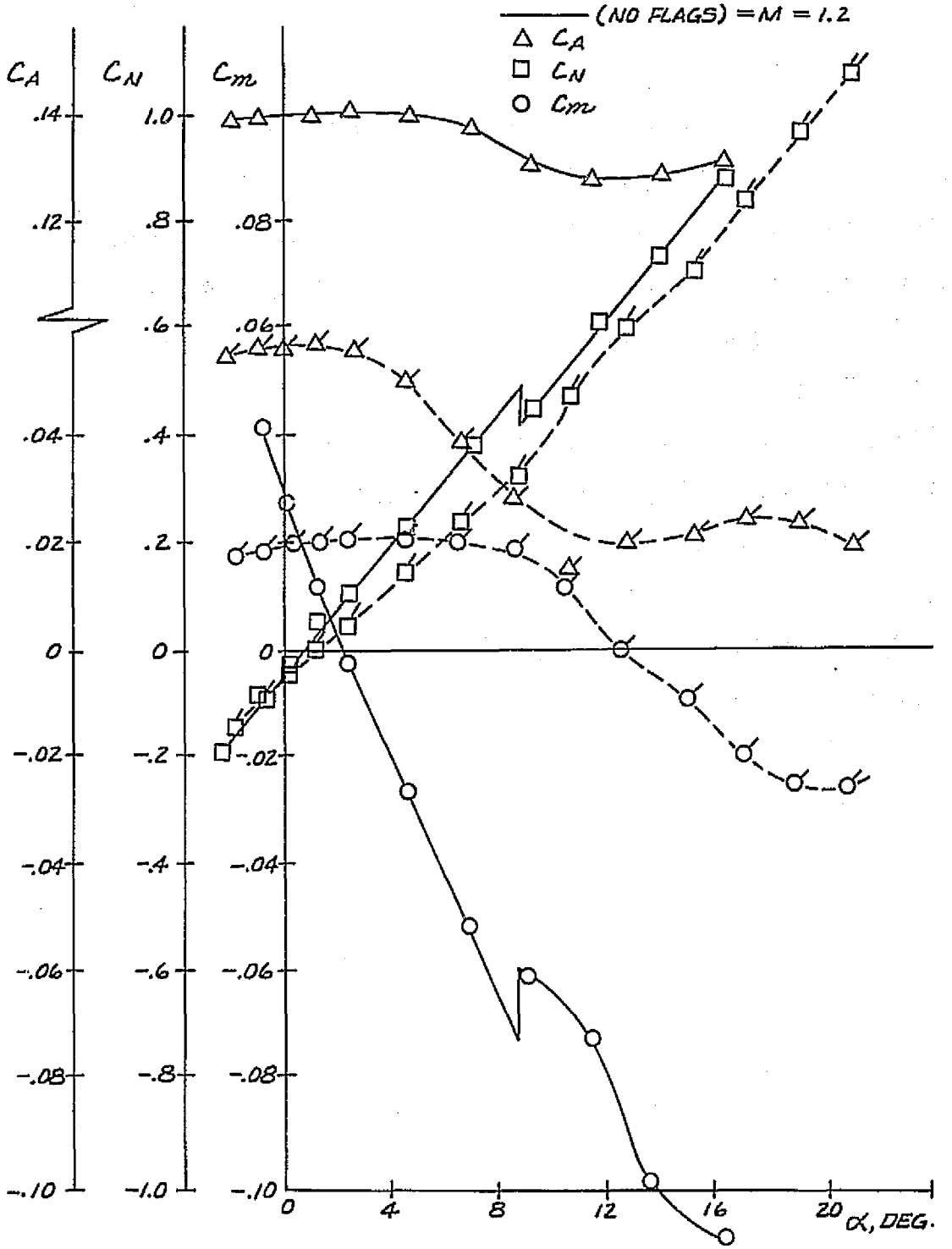

Figure 6 Typical Static Data (Ref. 24)

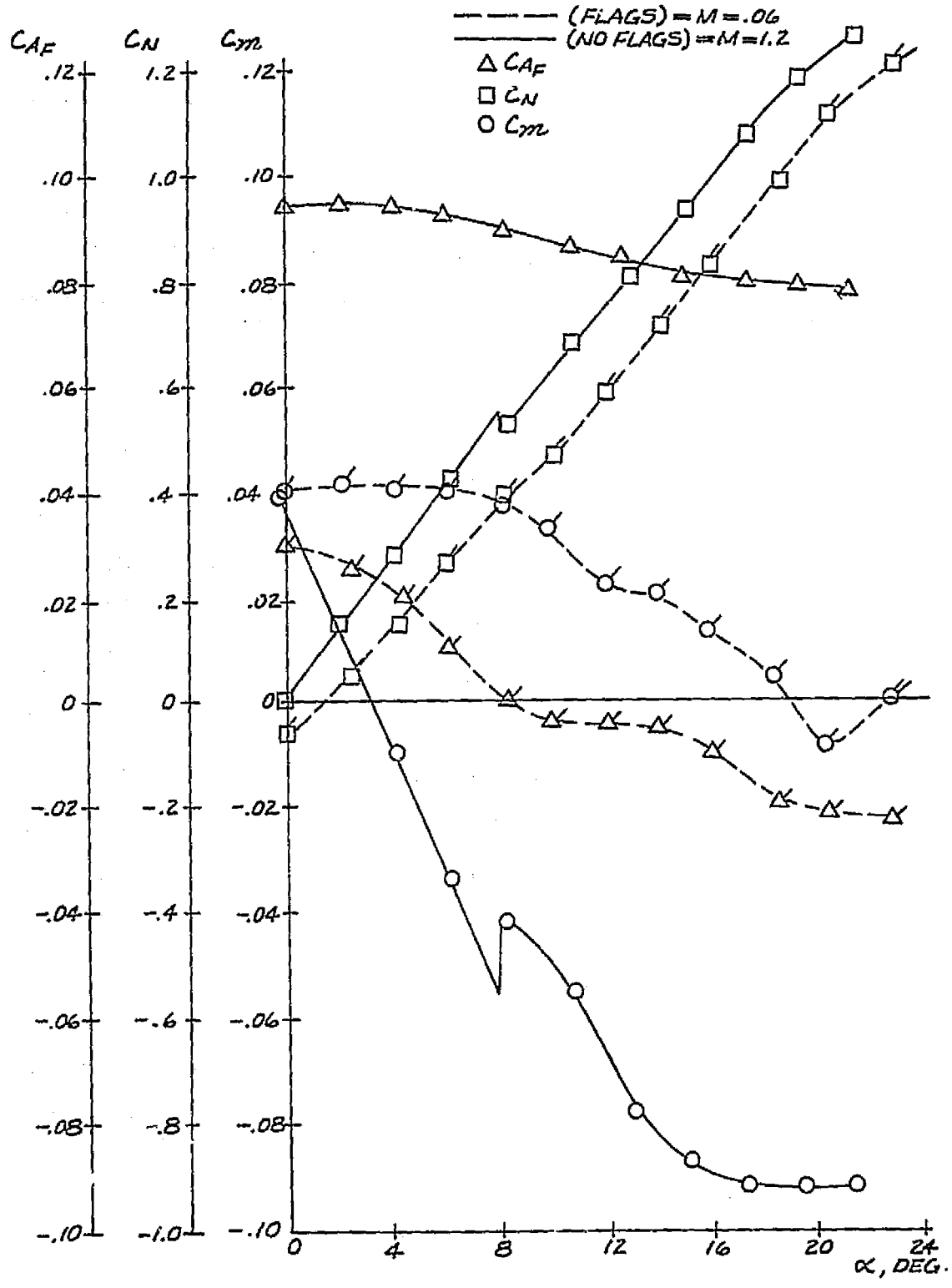

Figure 7 Typical Static Data (Ref. 25)

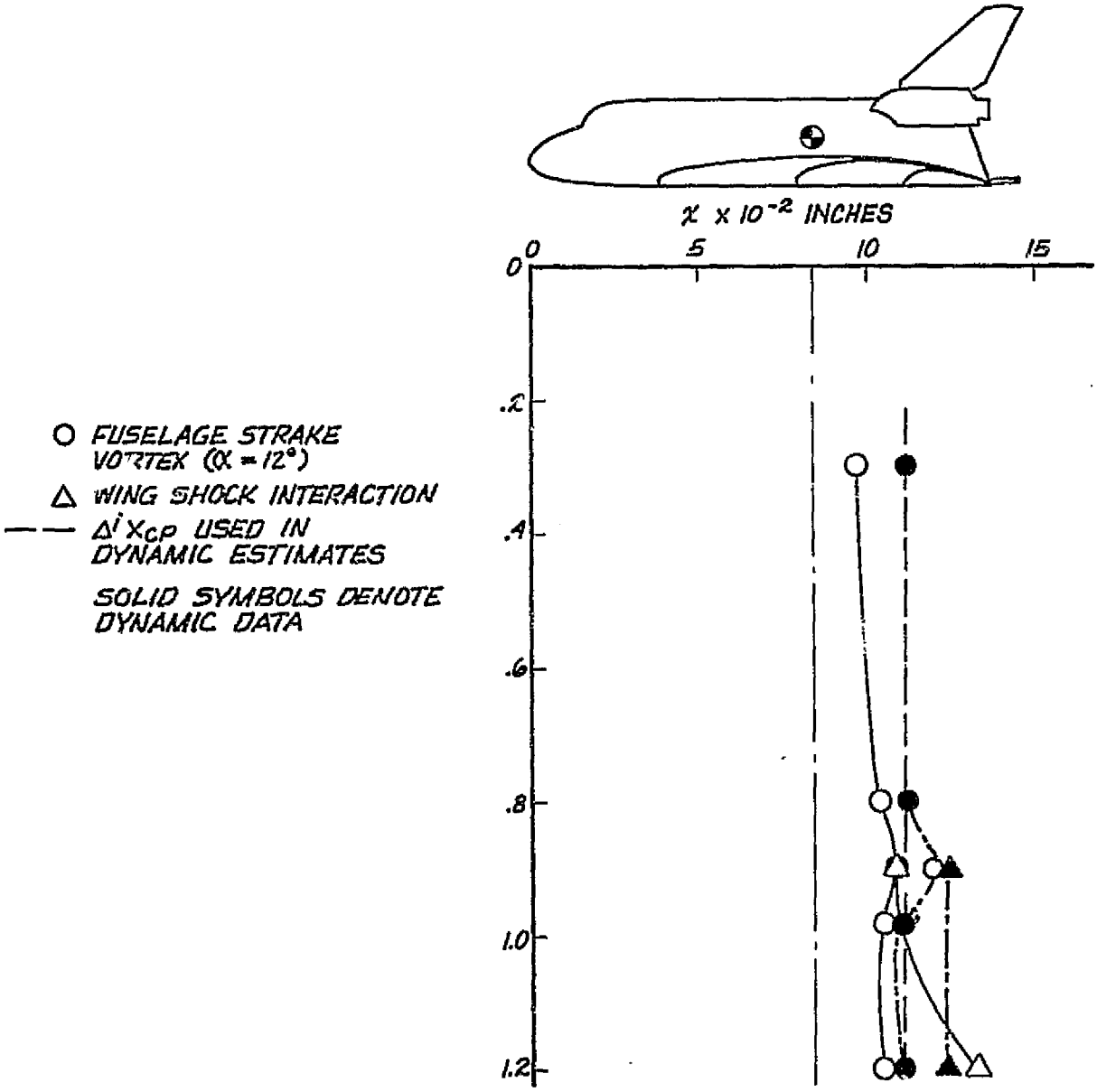

Figure 8 Induced Load Locations

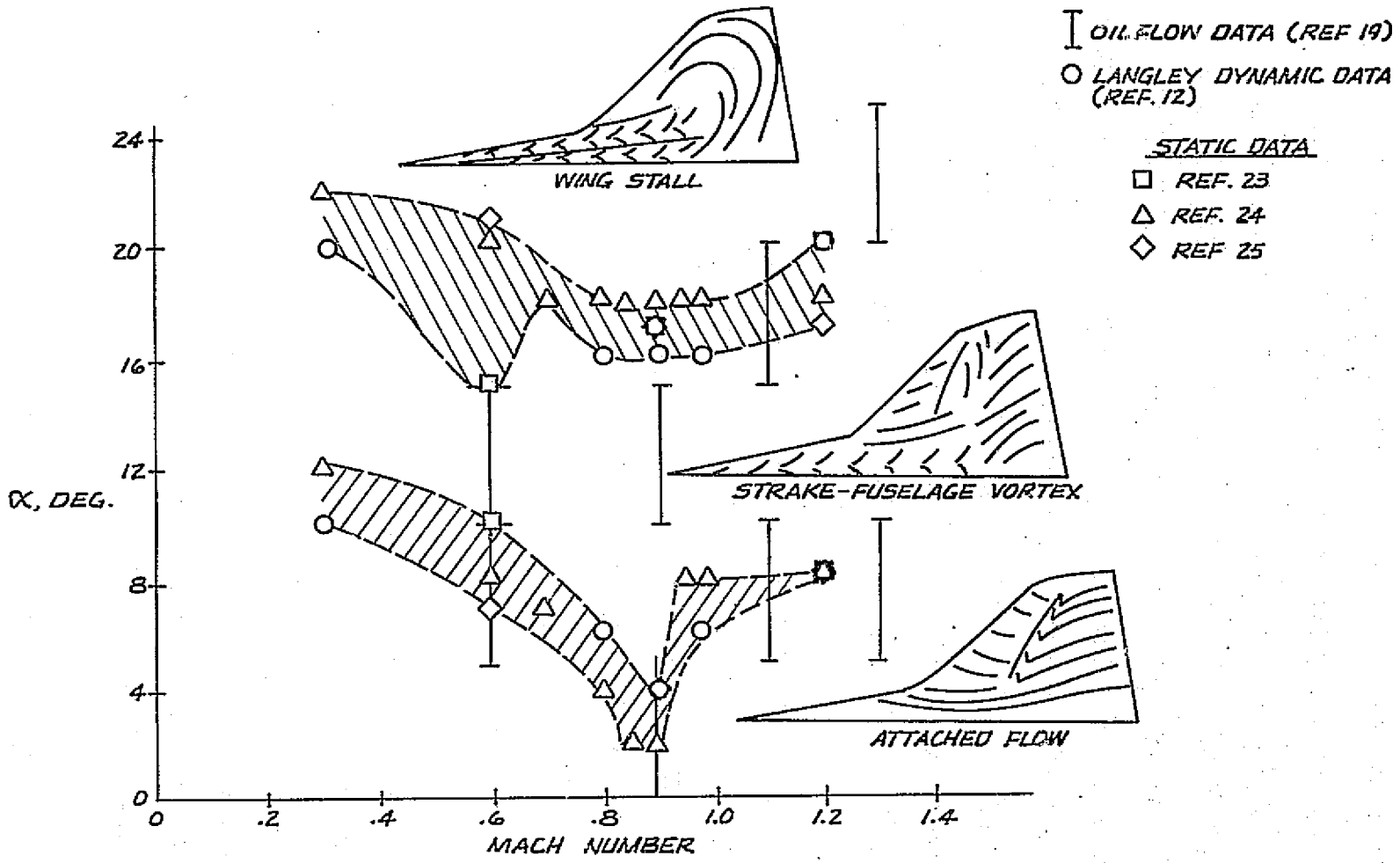

Figure 9 Correlation of Data Nonlinearities with Oil Flow Results

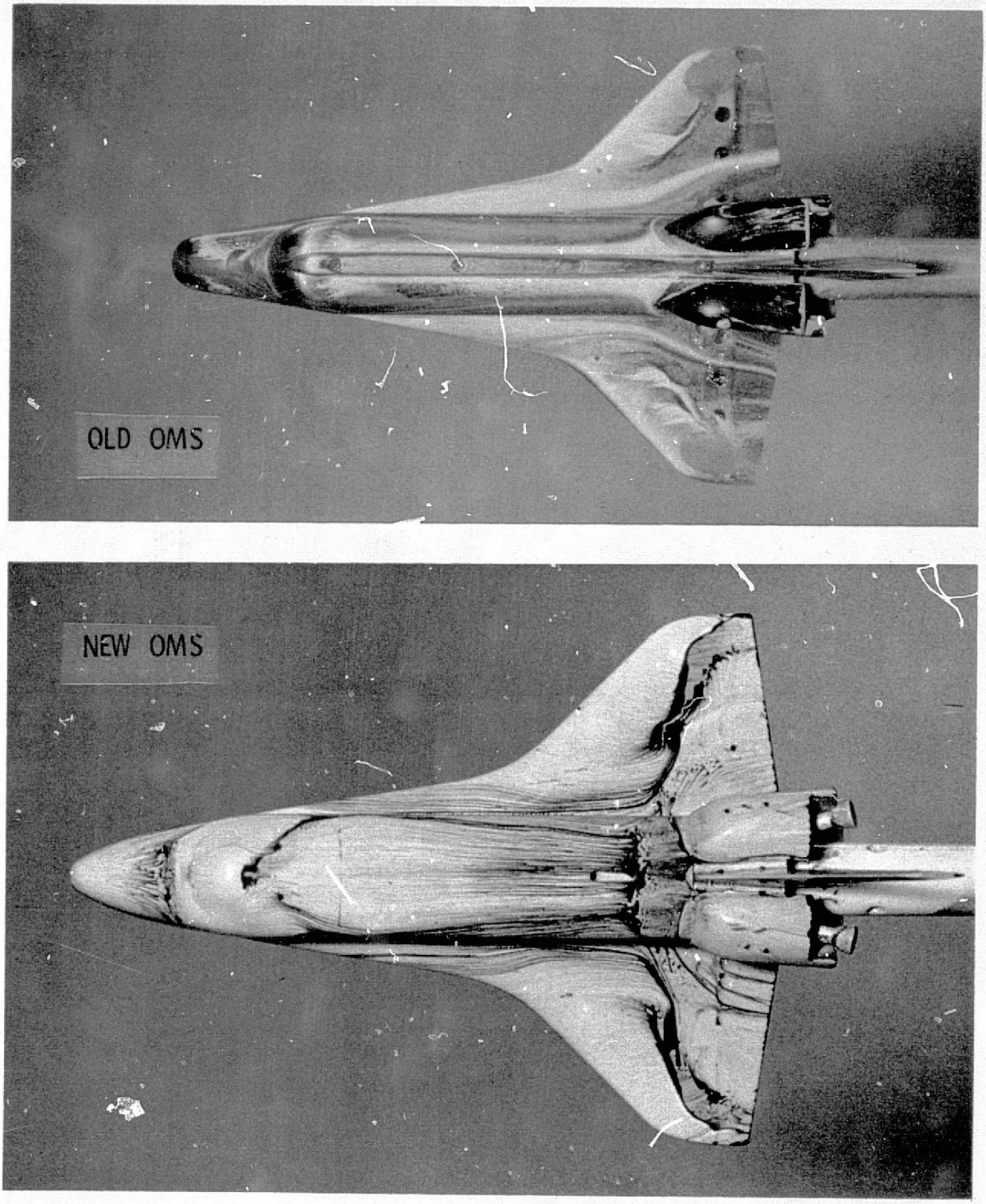

Figure 10 Effect of OMS Pod Configuration on Orbiter Flow Patterns at $M = 1.2$, $\alpha = 0$

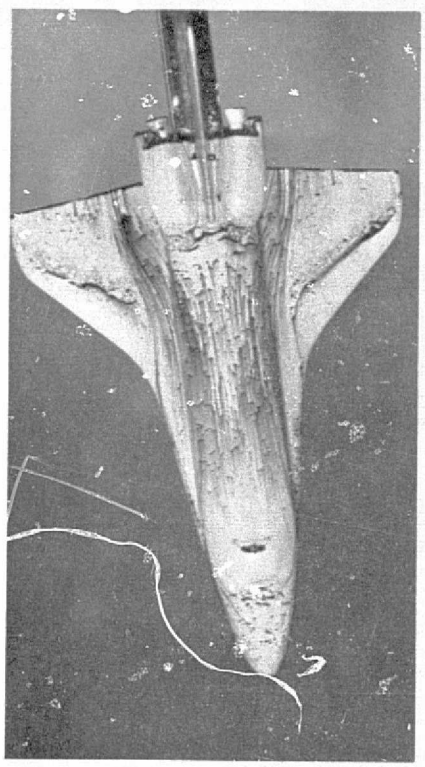

a. M = 1.2, $\alpha = 0$

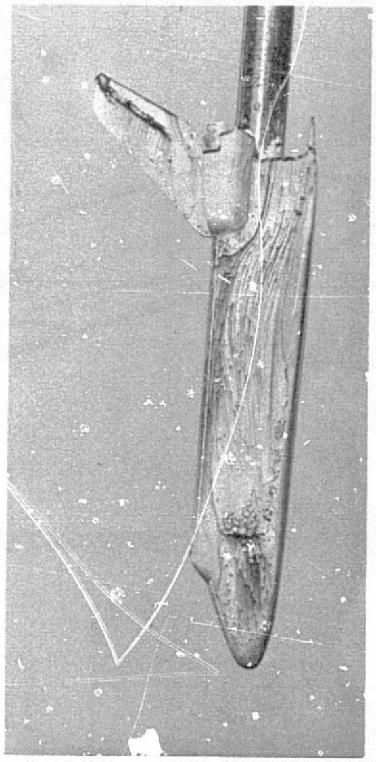

b. M = 0.6, $\alpha = 0$

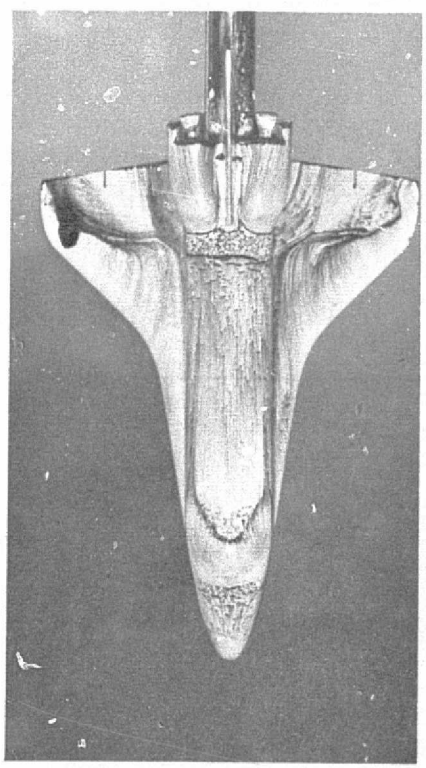

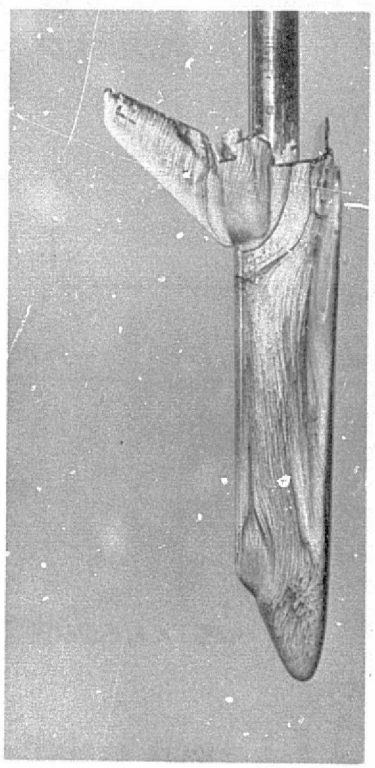

Figure 11 OMS Pod-Wing Flow Interference

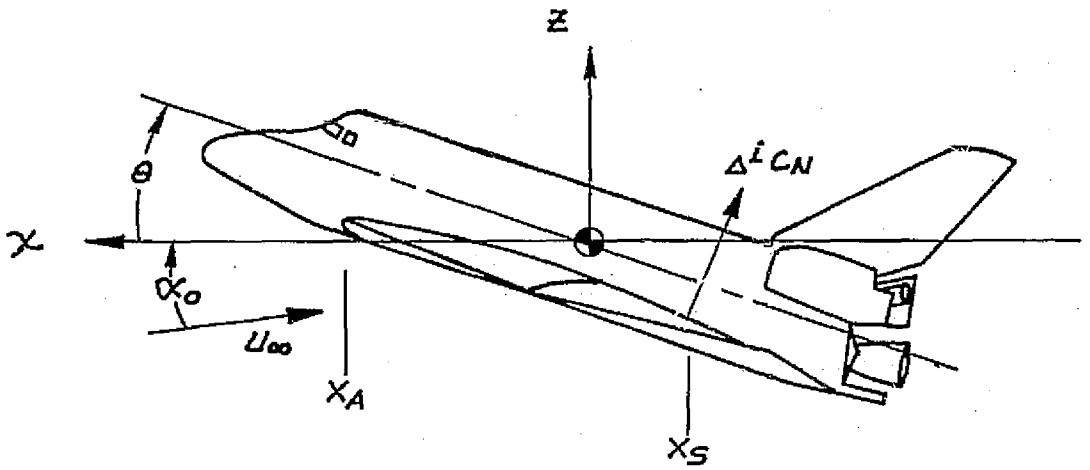

a) COORDINATE SYSTEM

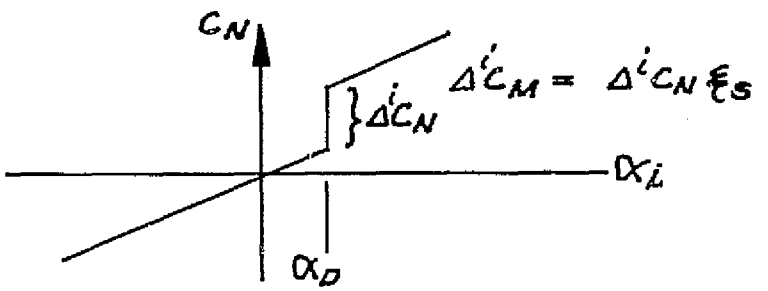

b) INDUCED LOAD

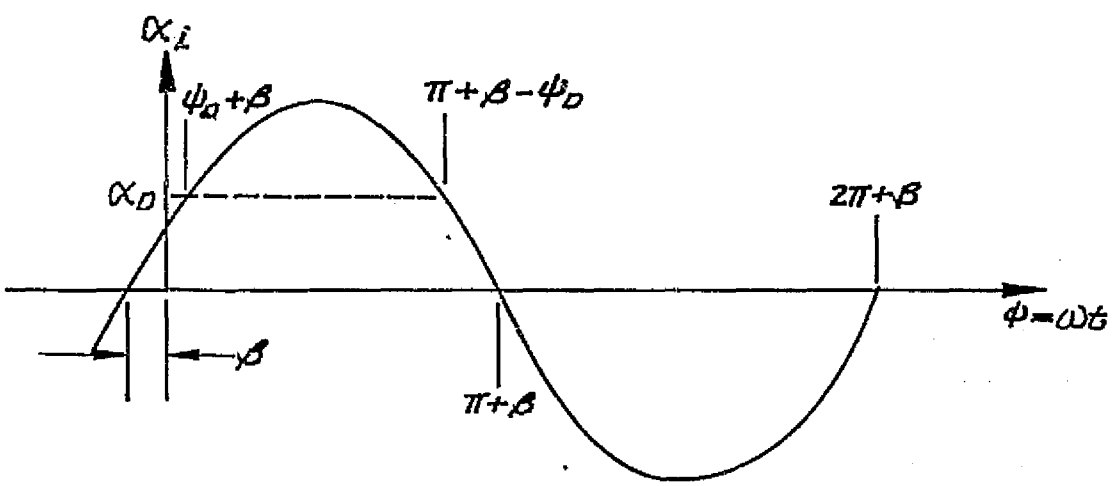

c) INSTANEOUS ANGLE OF ATTACK

Figure 12 Definition of Terms

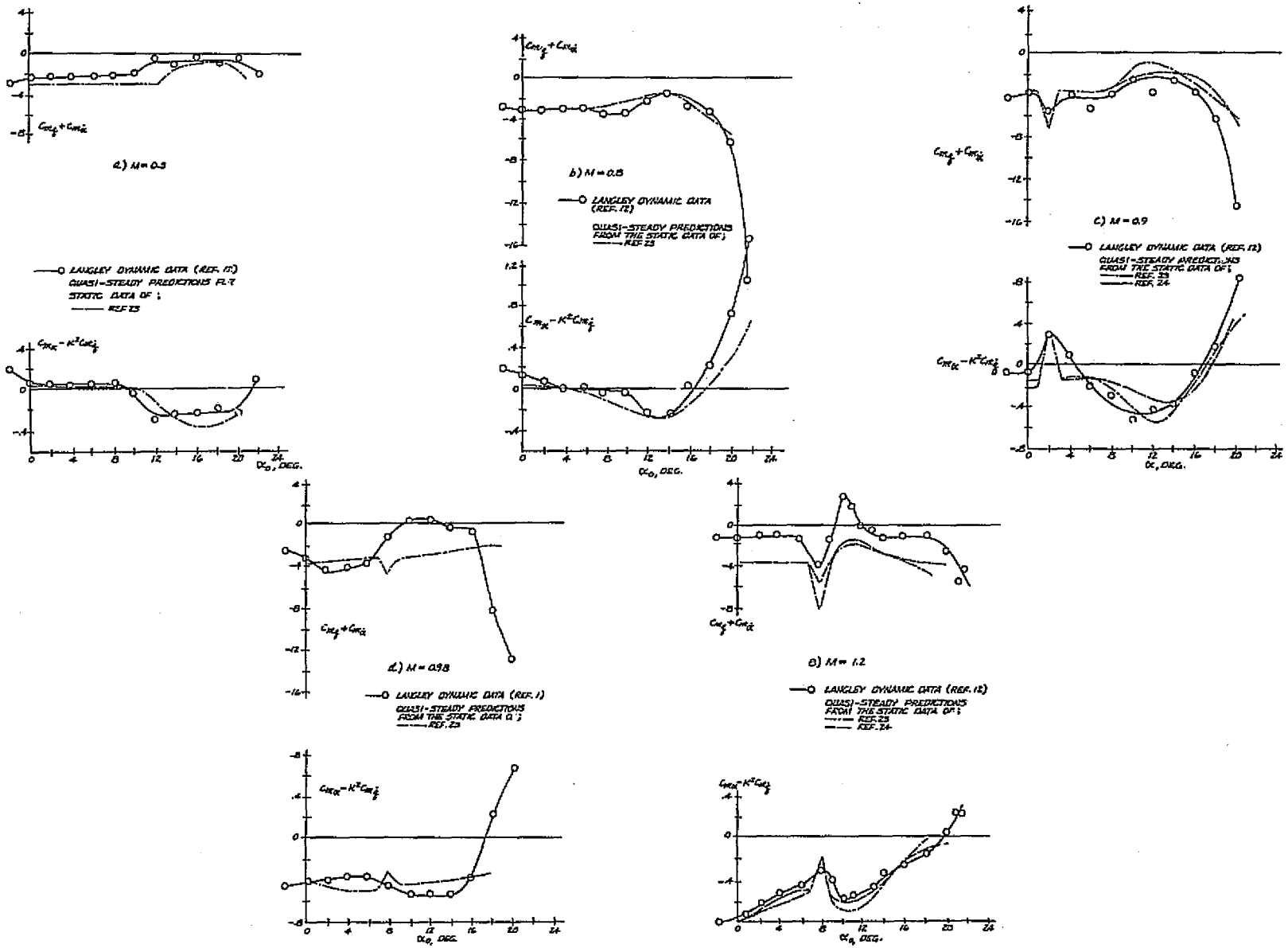

Figure 13 Comparison of Quasi-steady Predictions with Orbiter Dynamic Stability Data

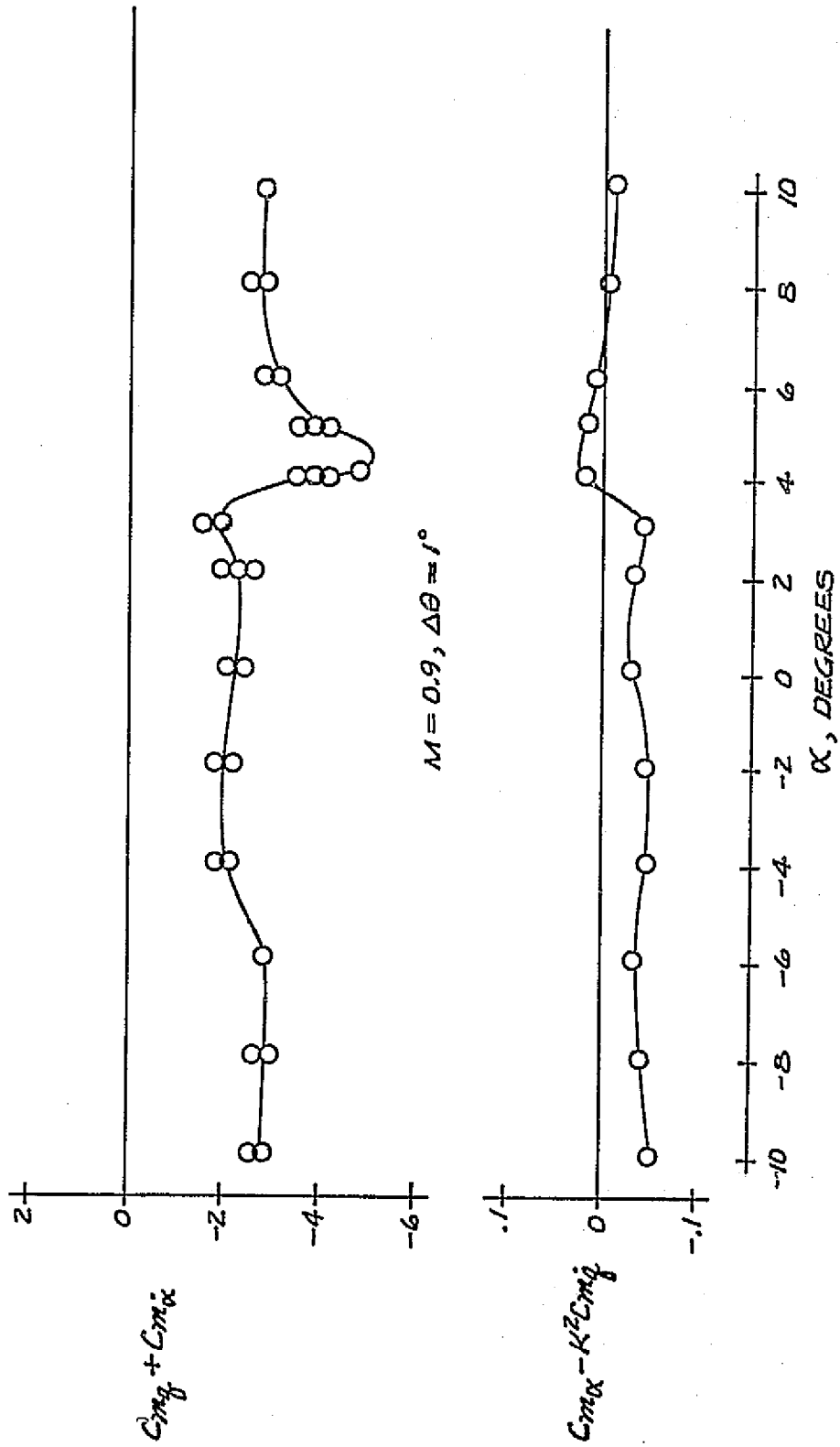

Figure 14 Typical Launch Configuration Dynamic Stability Data at M = 0.9

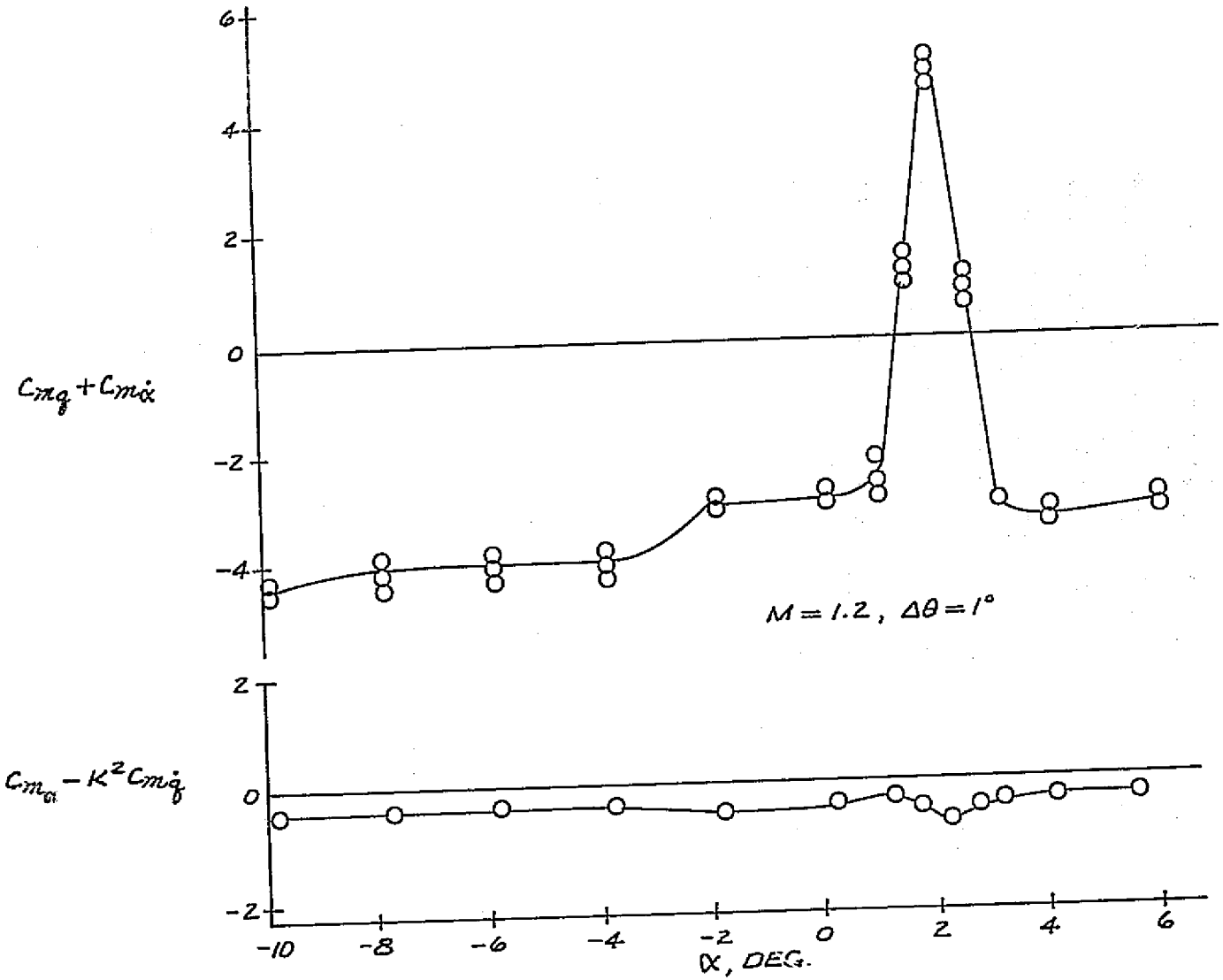

Figure 15 Typical Launch Configuration Dynamic Stability Data at M = 1.2

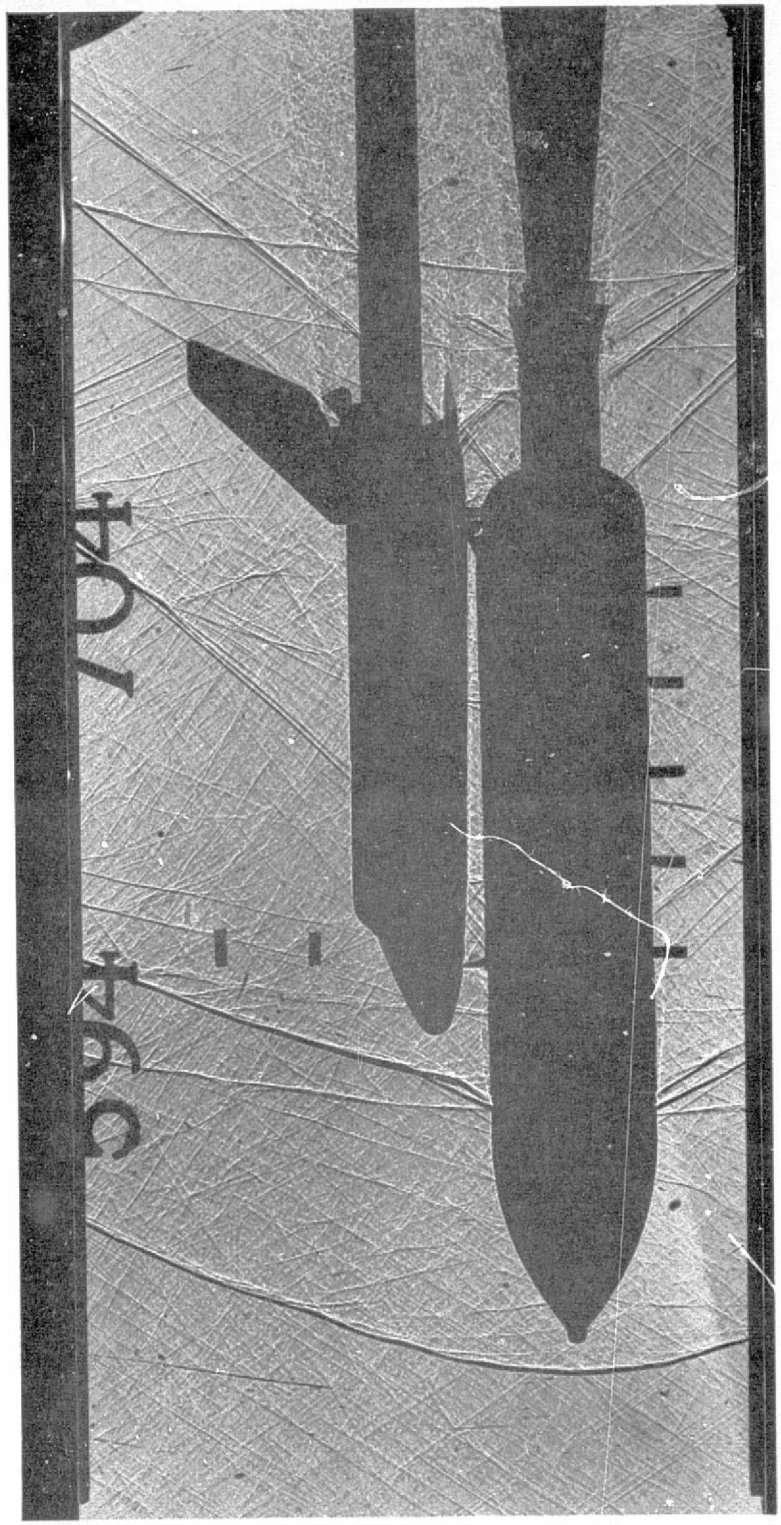

Figure 16 Shadowgraph of Launch Configuration at M = 1.2

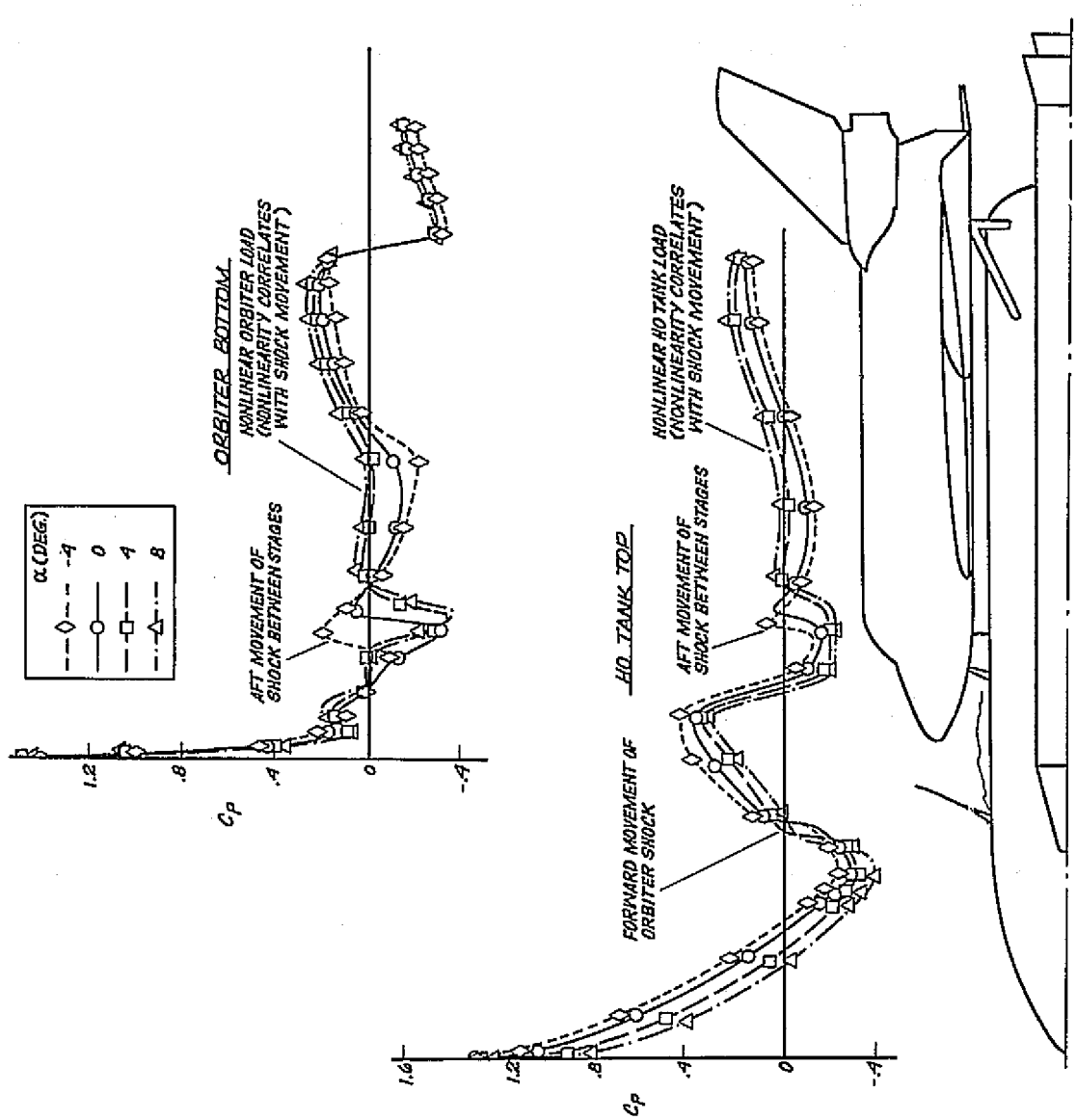

Figure 17 Pressure Distributions Between Stages of Launch Configuration at M = 1.2

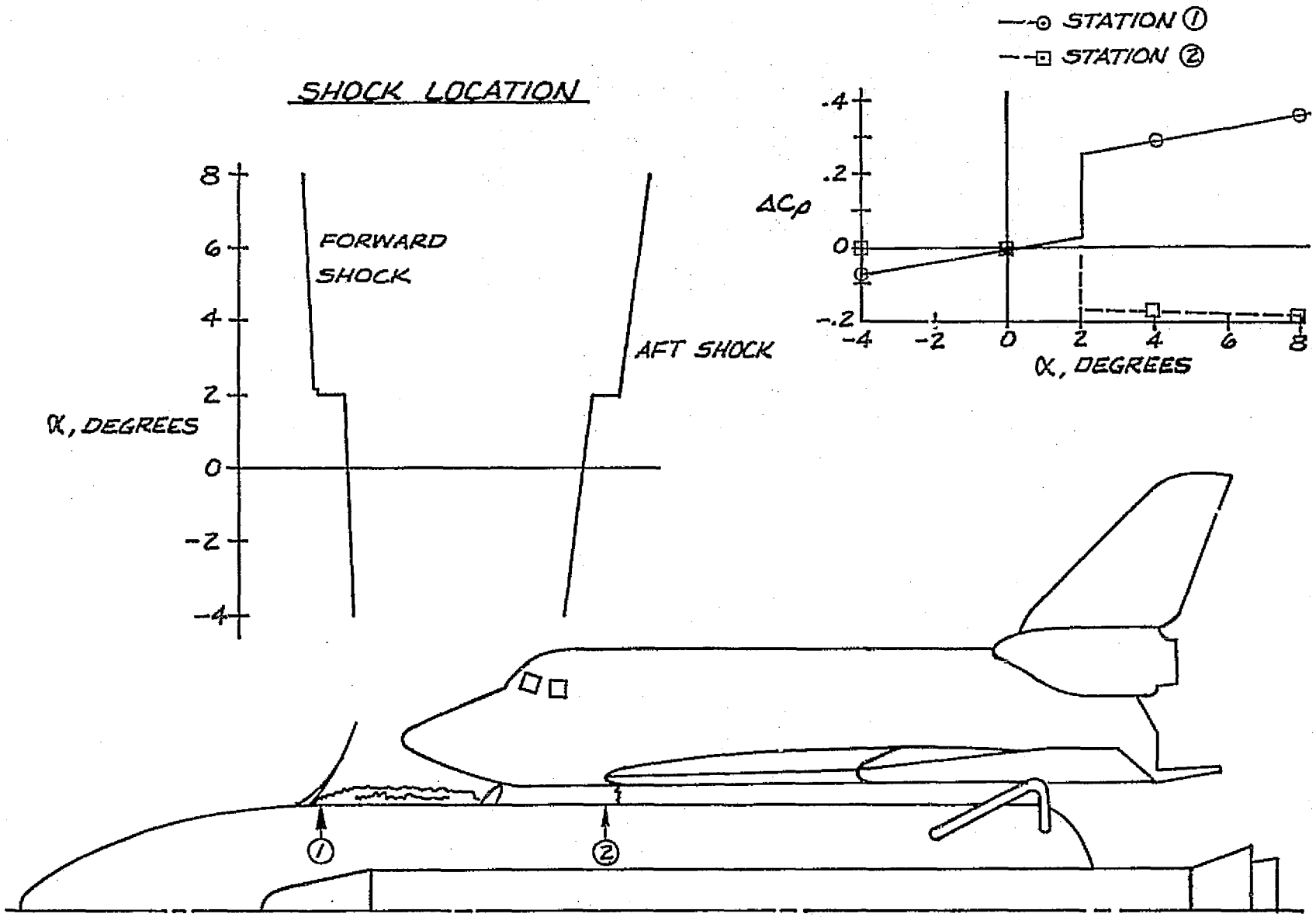

Figure 18 Correlation of Shock Locations and Pressure Jump at M = 1.2

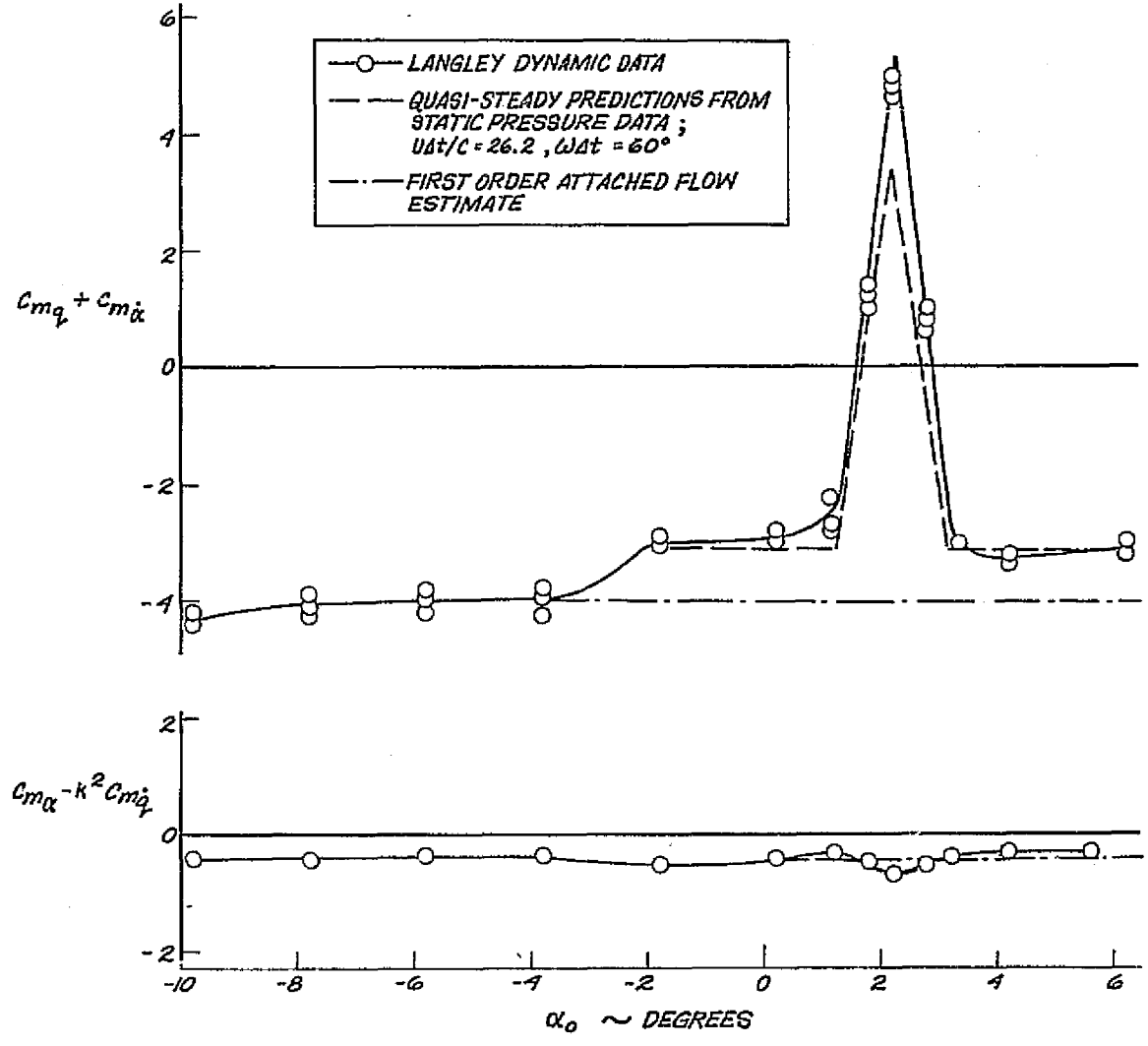

Figure 19 Comparison of Quasi-steady Predictions with Launch Configuration Dynamic Moment Derivative Measurements at M = 1.2

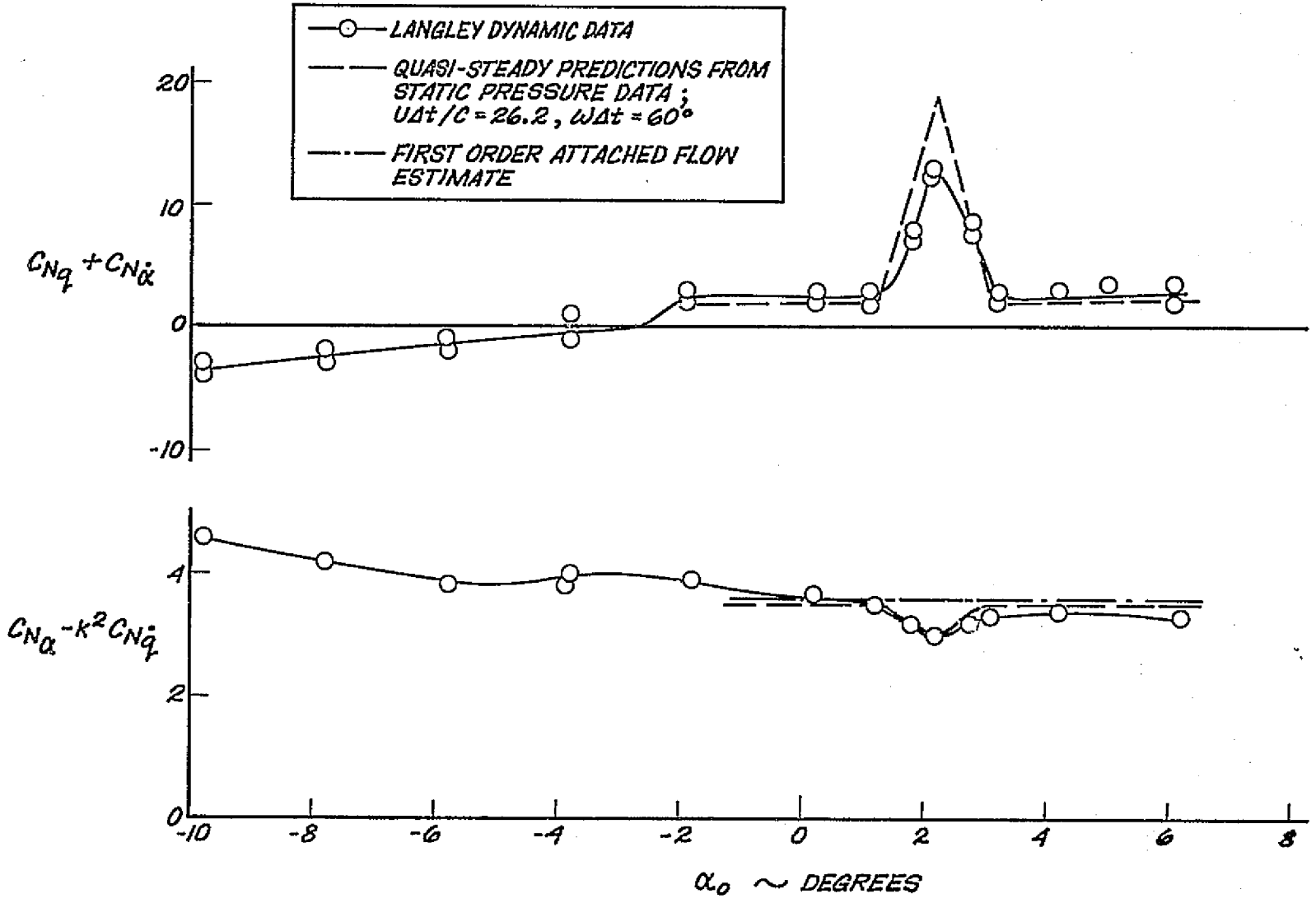

Figure 20 Comparison of Quasi-steady Predictions with Launch Configuration Dynamic Normal Force Derivative Measurements at M = 1.2

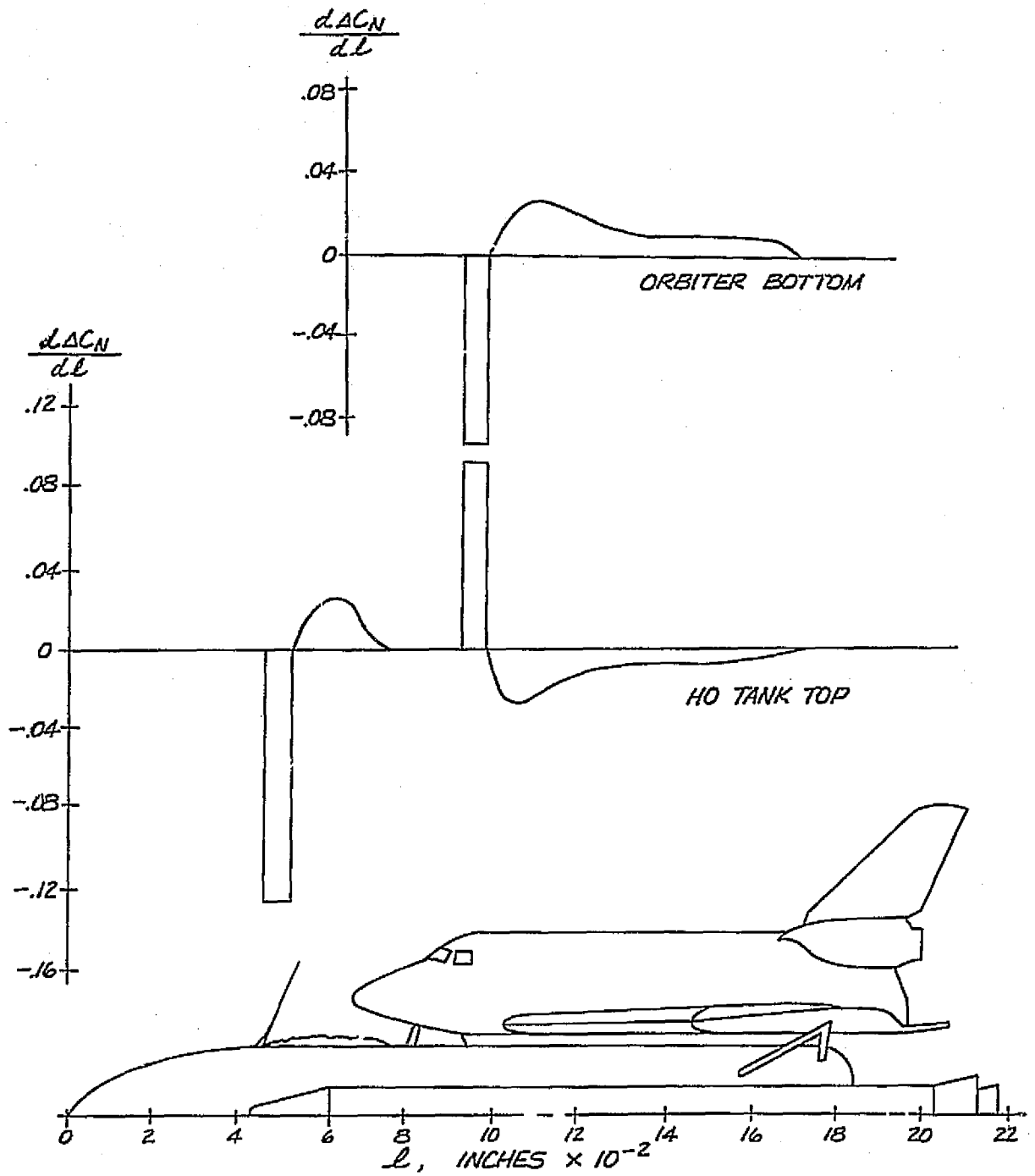

Figure 21 Jump Induced Load Distribution for Inlet Flow, M = 1.2

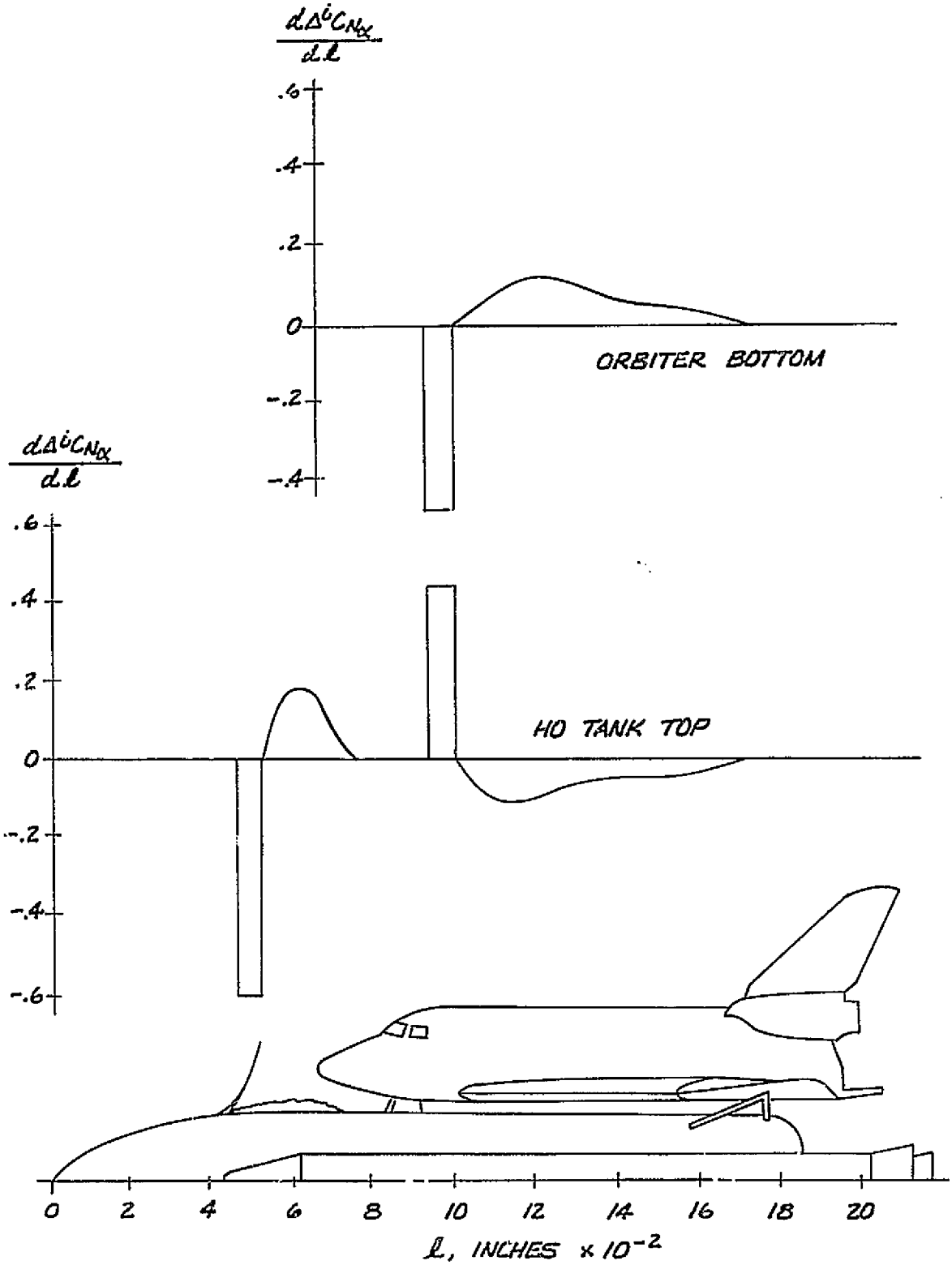

Figure 22 Induced Normal Force Derivative Distribution for Inlet Flow, M = 1.2

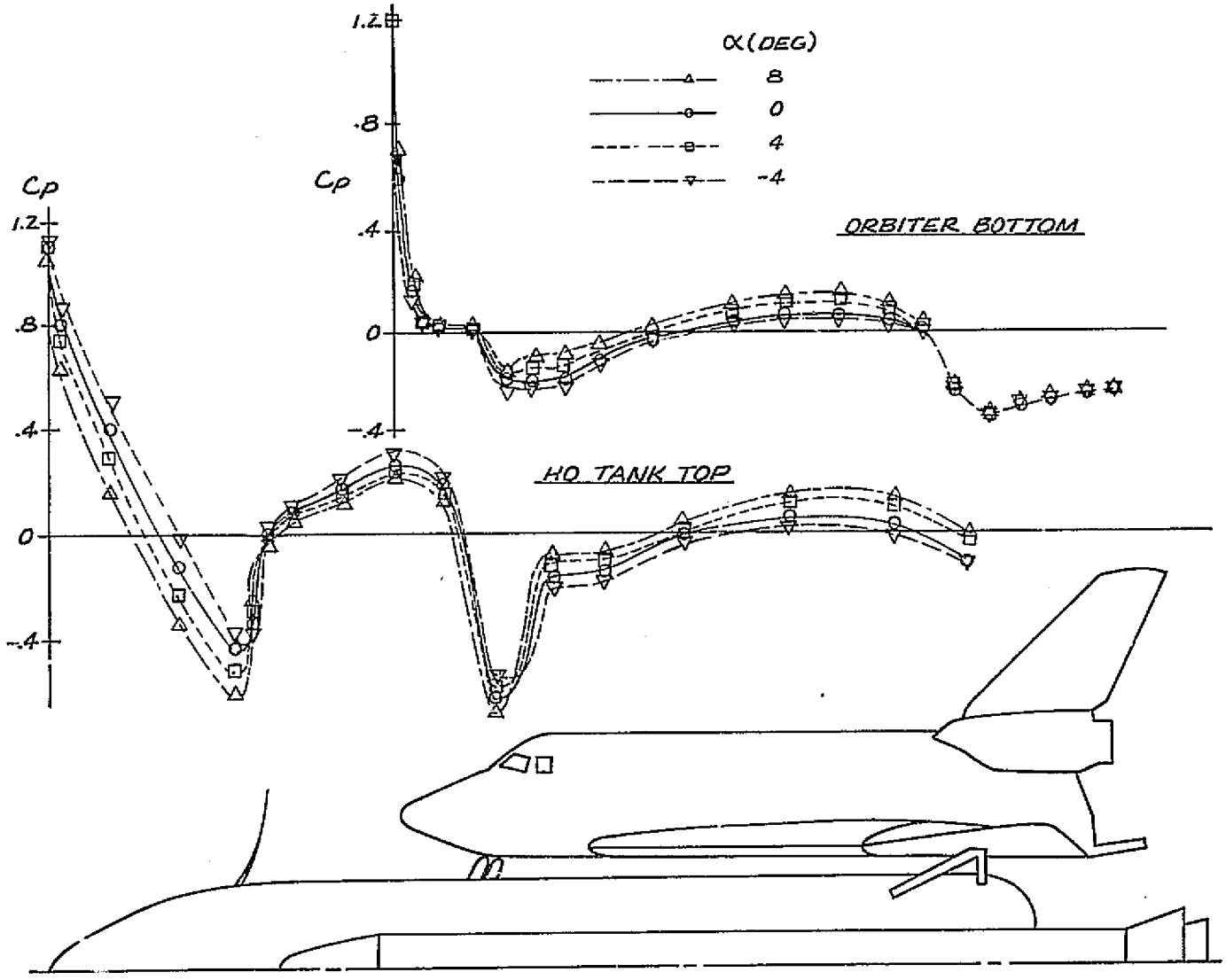

Figure 23 Pressure Distribution Between Stages of Launch Configuration, M = 0.9

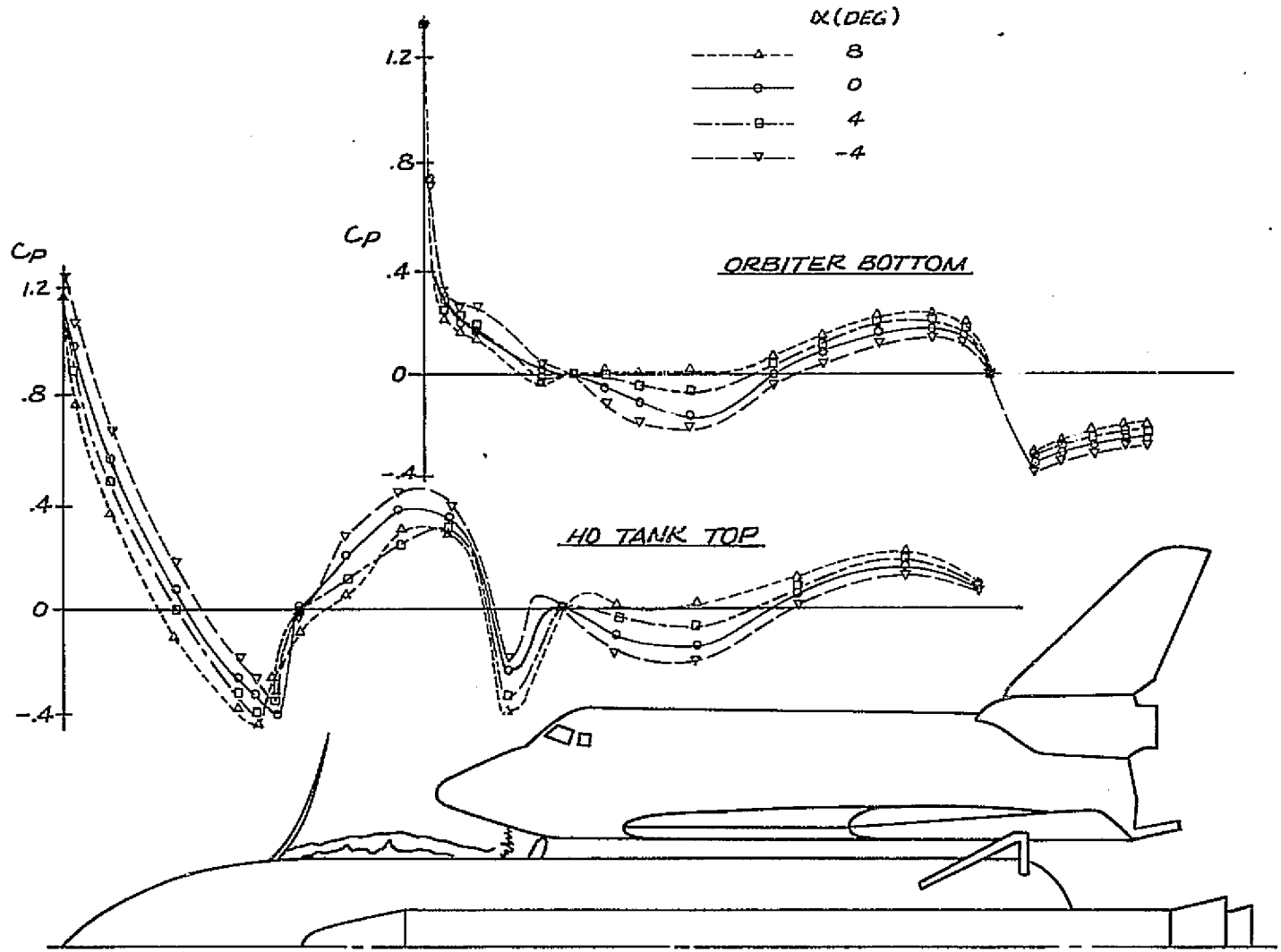

Figure 24 Pressure Distribution Between Stages of Launch Configuration, M = 1.1

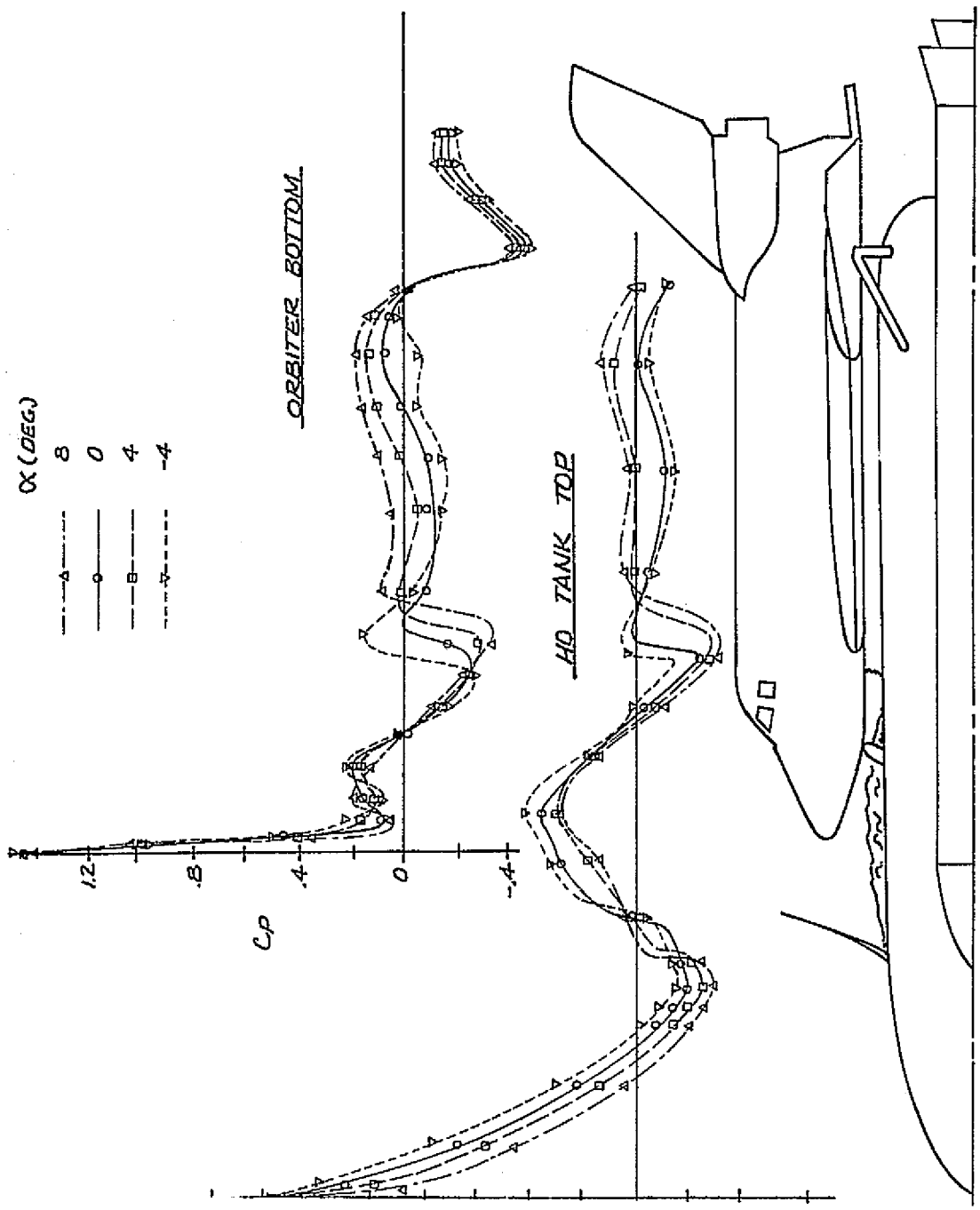

Figure 25 Pressure Distribution Between Stages of Launch Configuration, M = 1.4

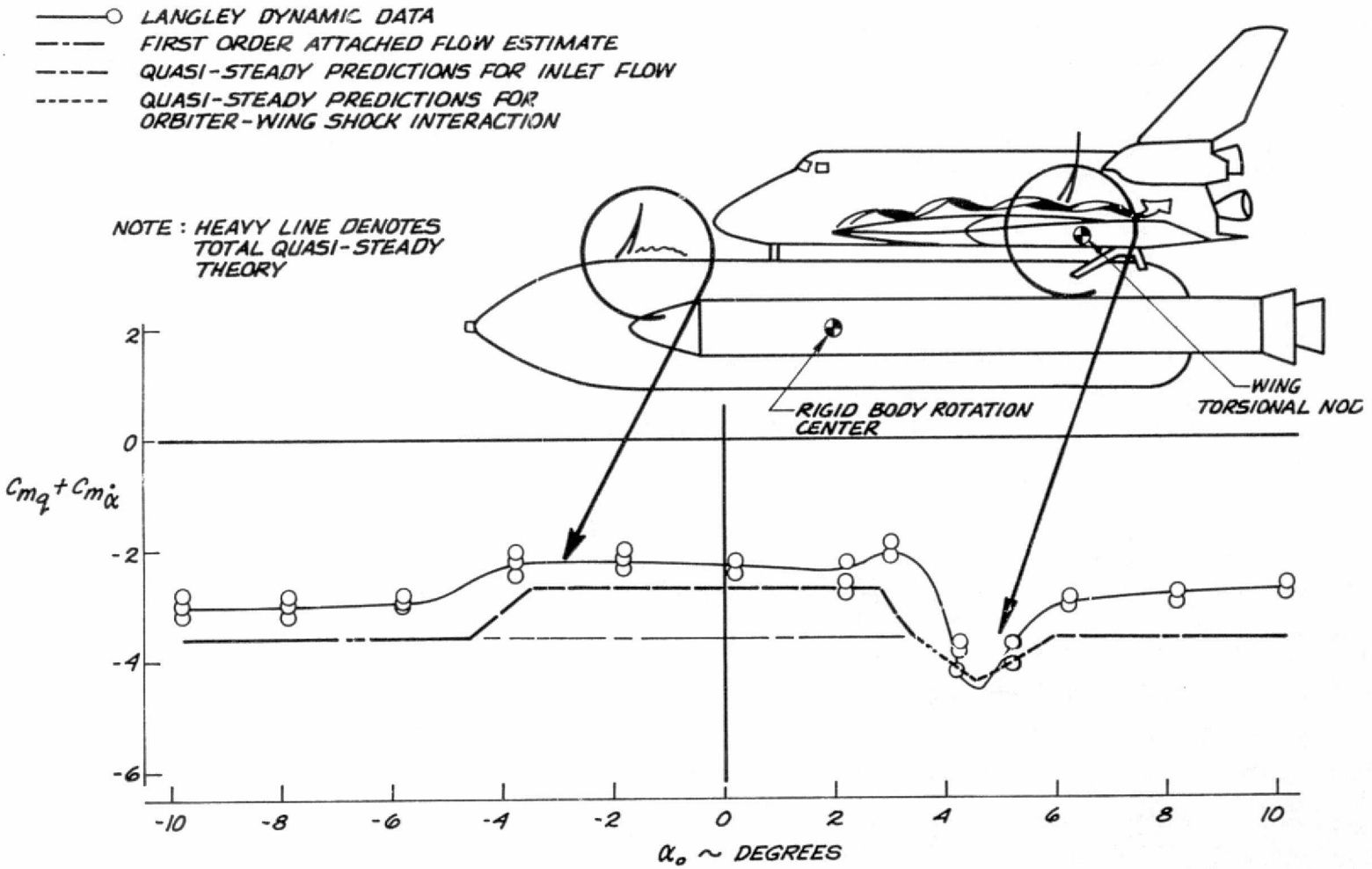

Figure 26 Effect of HO Tank Separation and Wing Shock Interaction on Lift-off Configuration Rigid Body Damping; M = 0.9

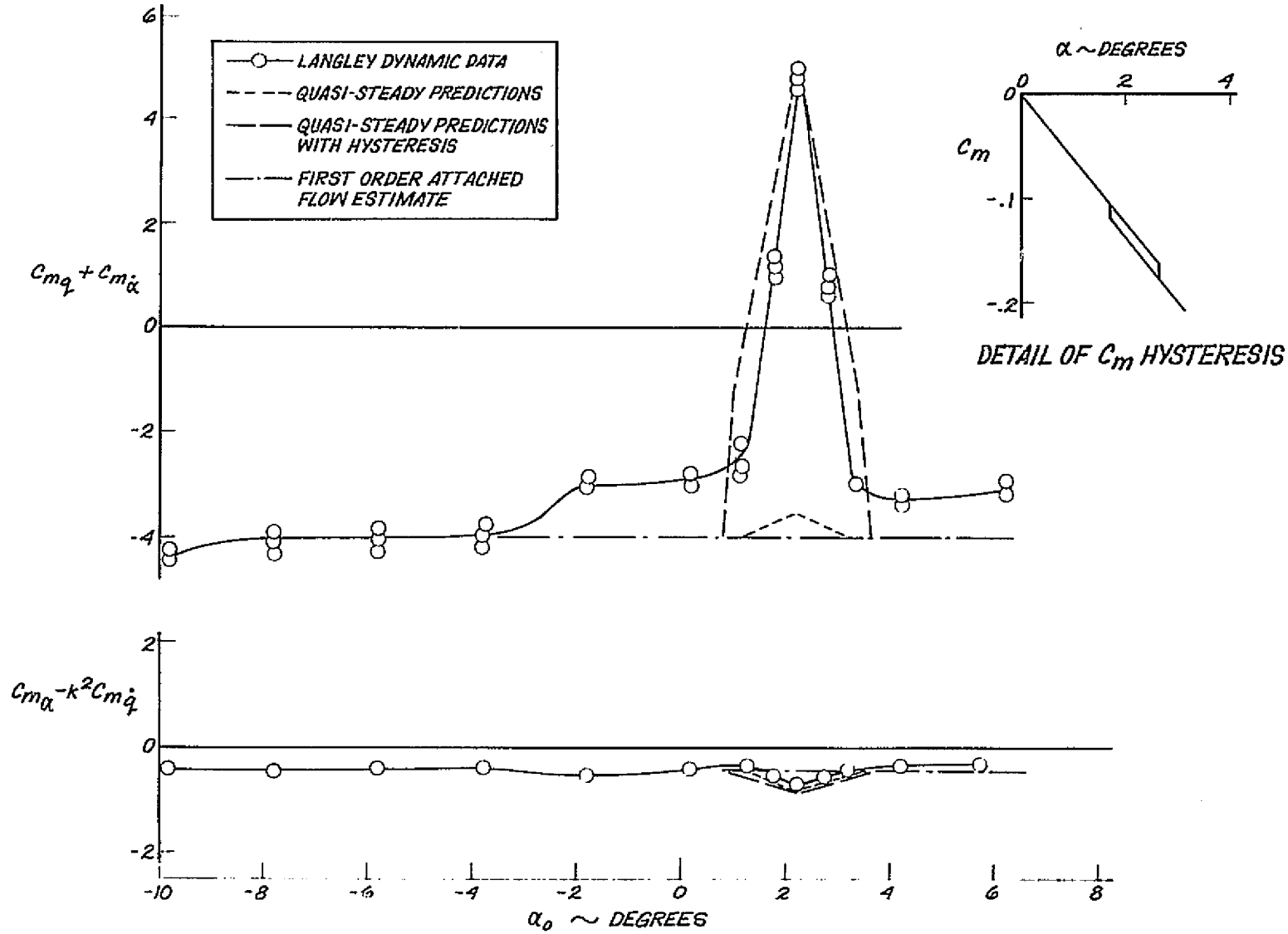

Figure 27 Comparison of Experimental Dynamic Data With Quasi-steady Predictions Assuming only Sudden Separation Effect (M = 1.2)

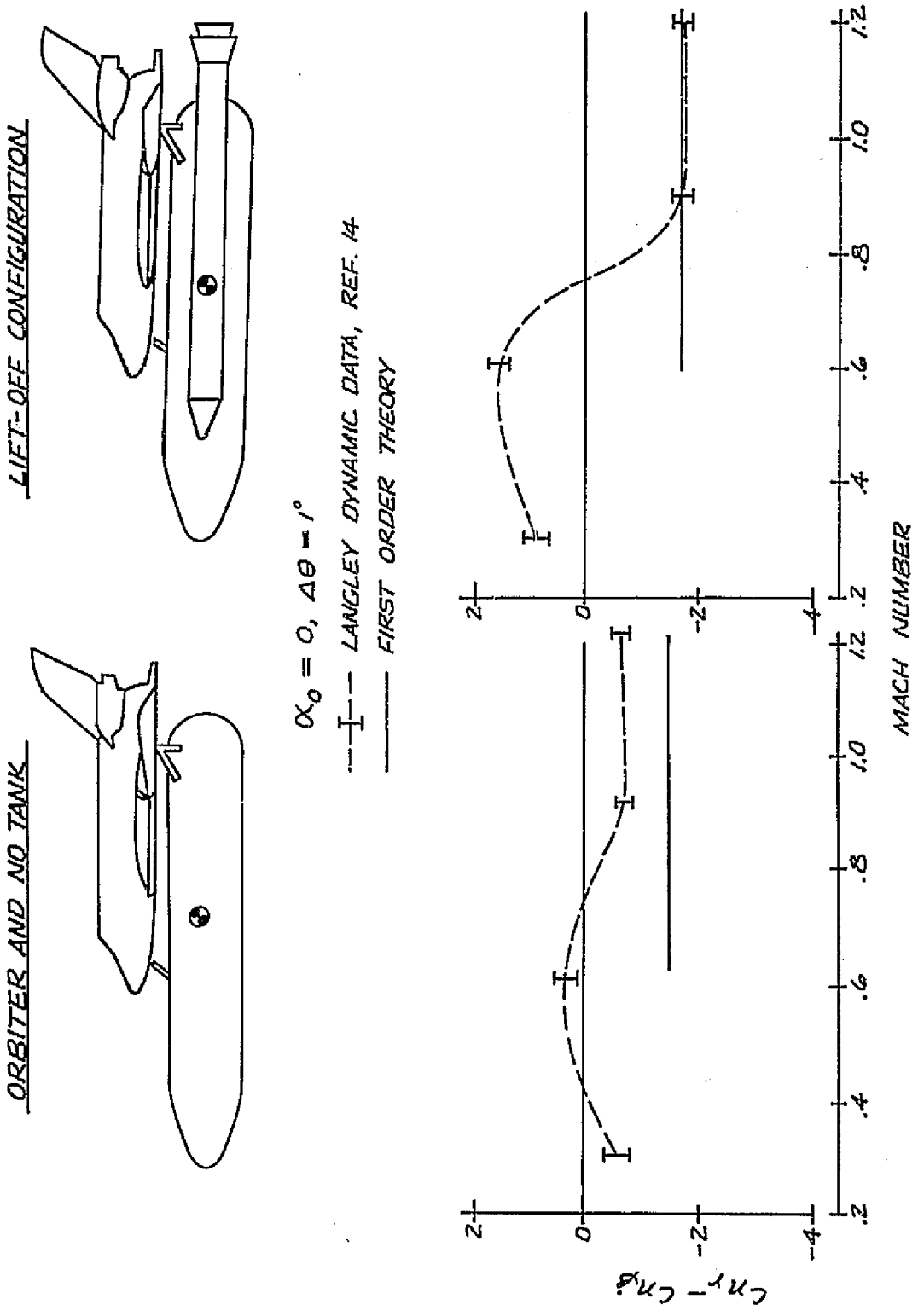

Figure 28 Yaw Damping of Launch Configuration

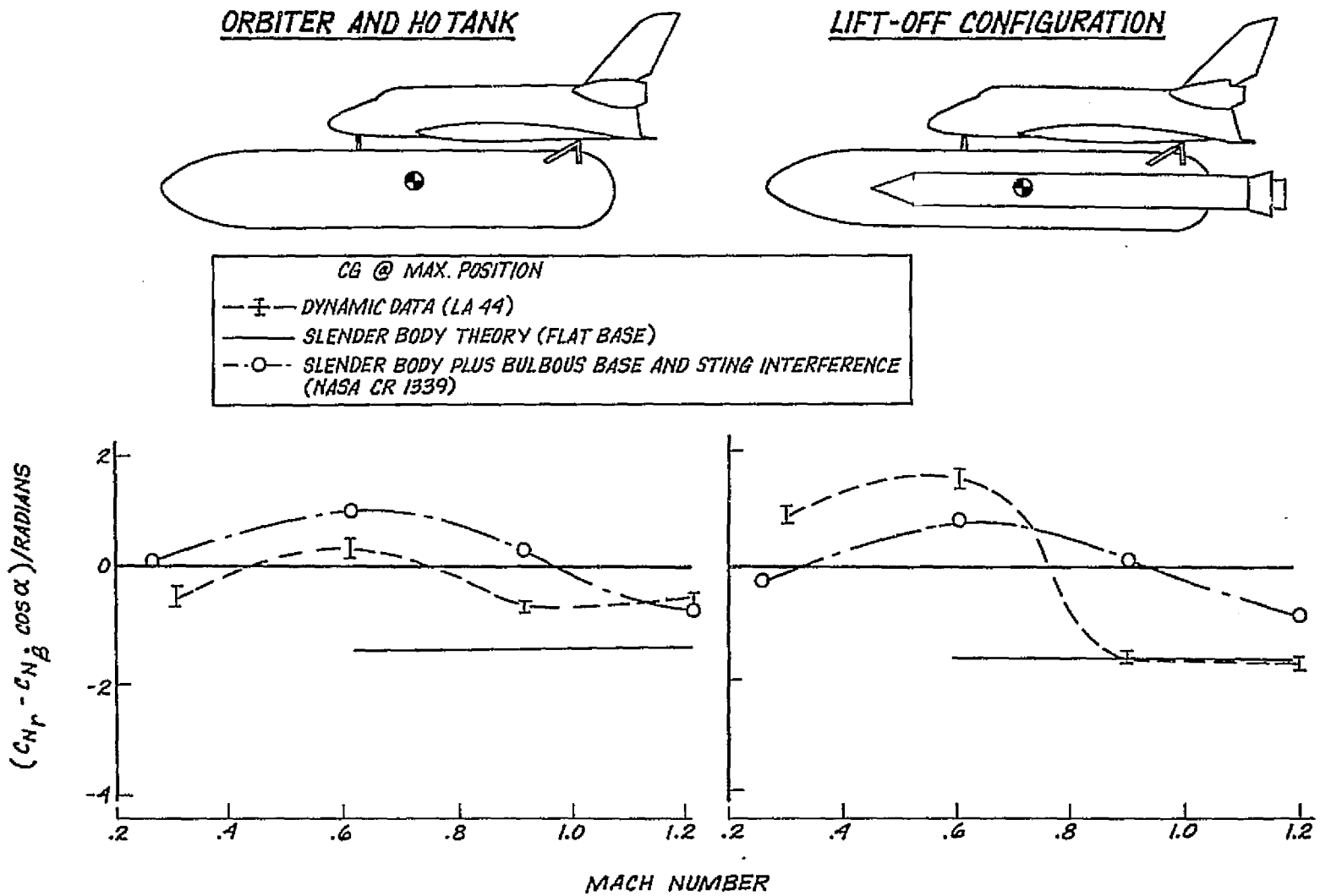

Figure 29 Effect of HO Tank Bulbous Base on Launch Configuration Dynamic Stability

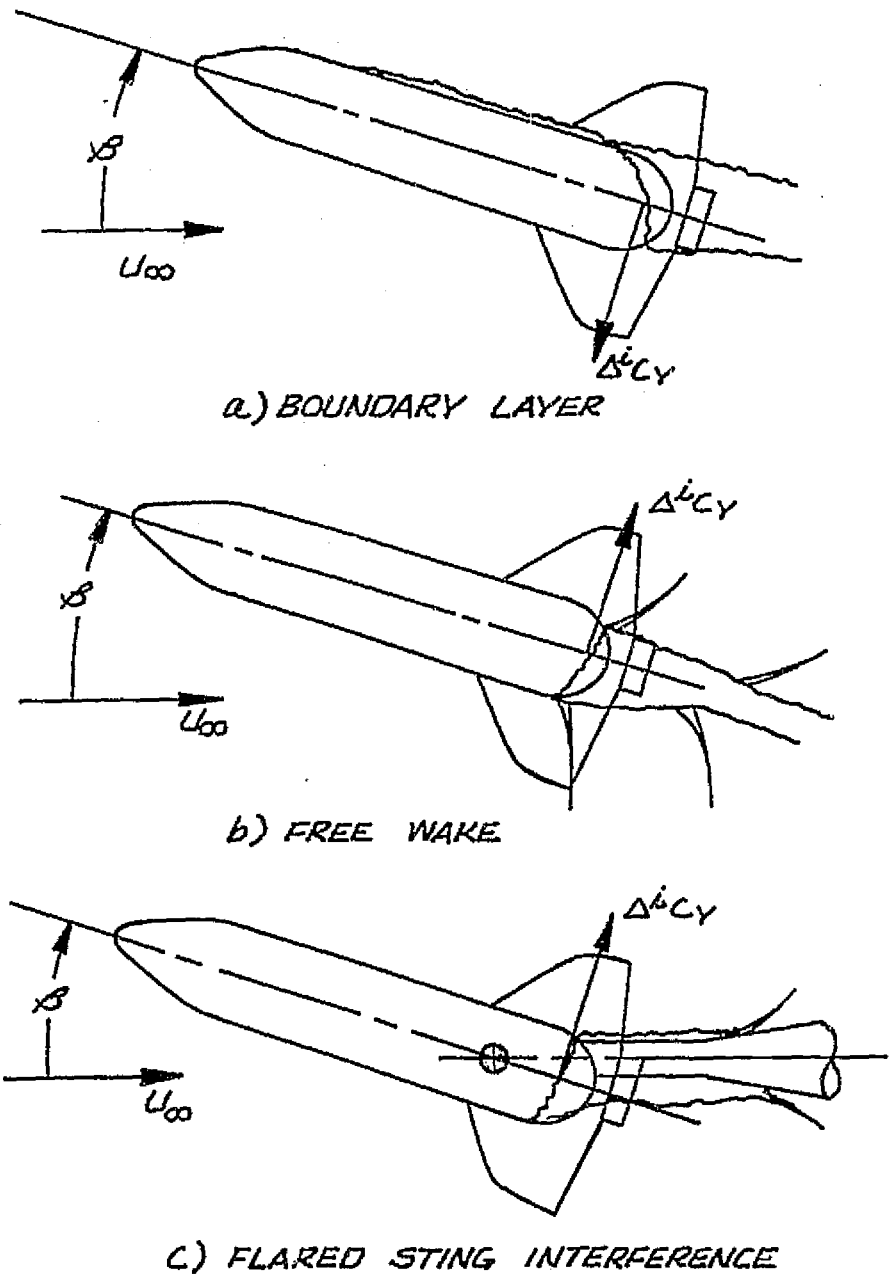

Figure 30 HO Tank Base Interference Effects

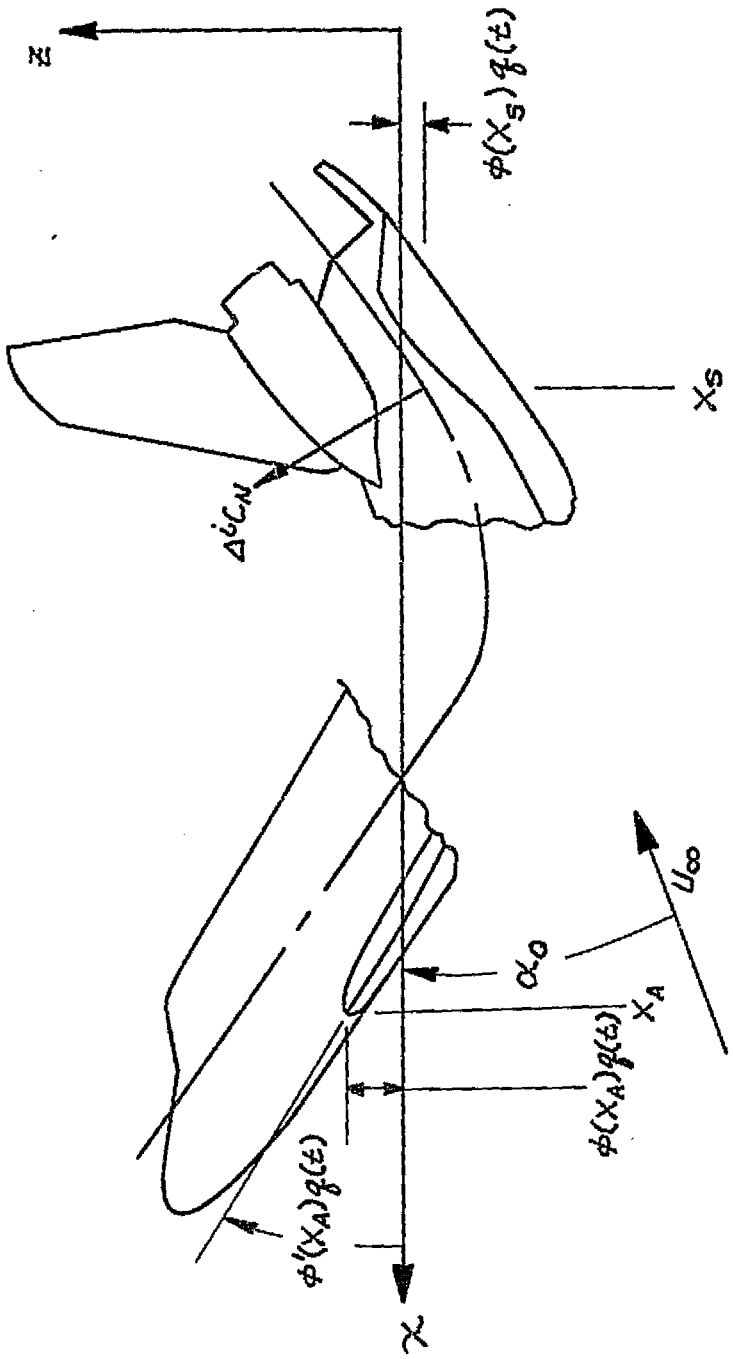

Figure 31 Coordinate System for Elastic Orbiter

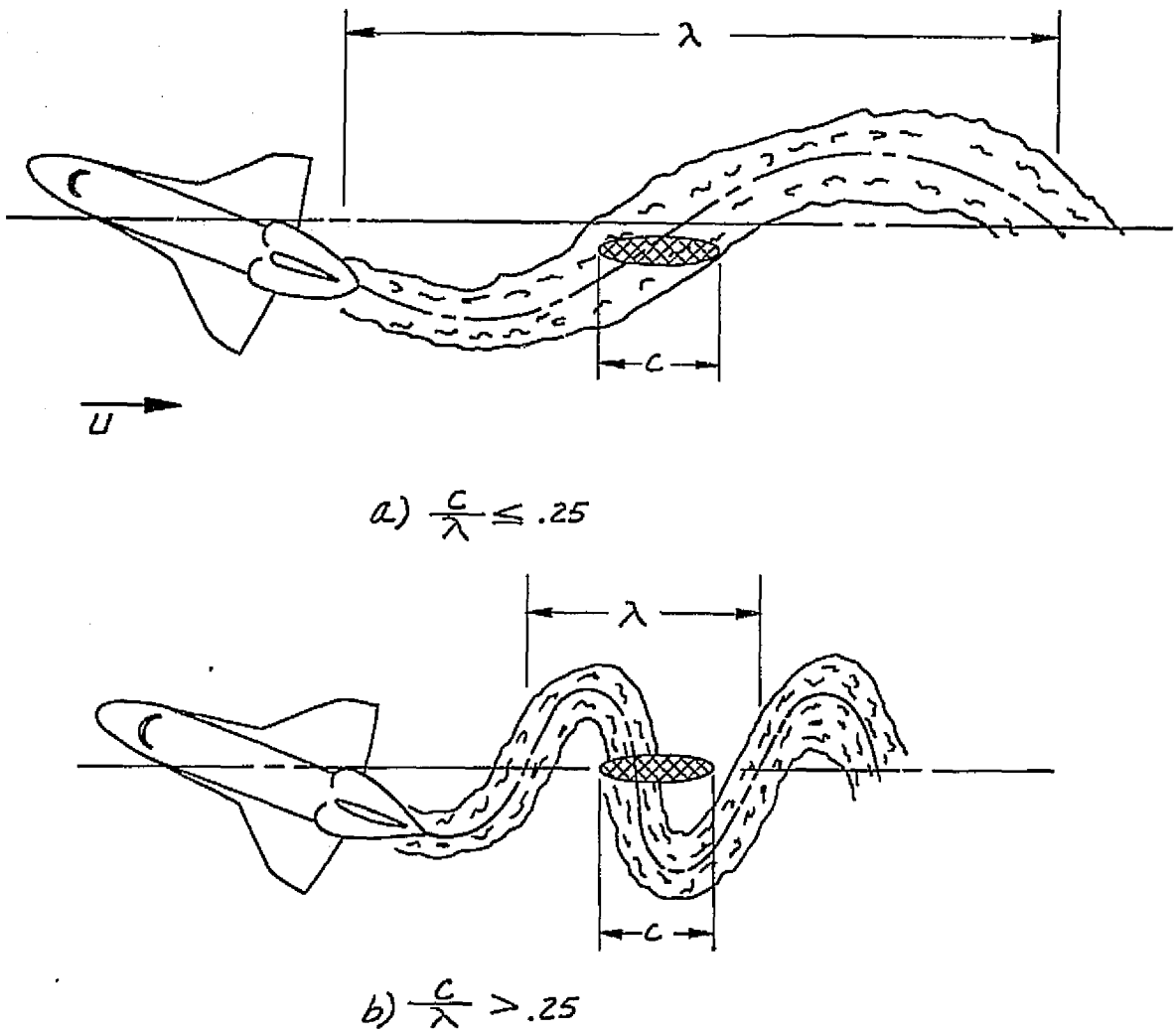

Figure 32 Limit of Quasi-Steady Theory

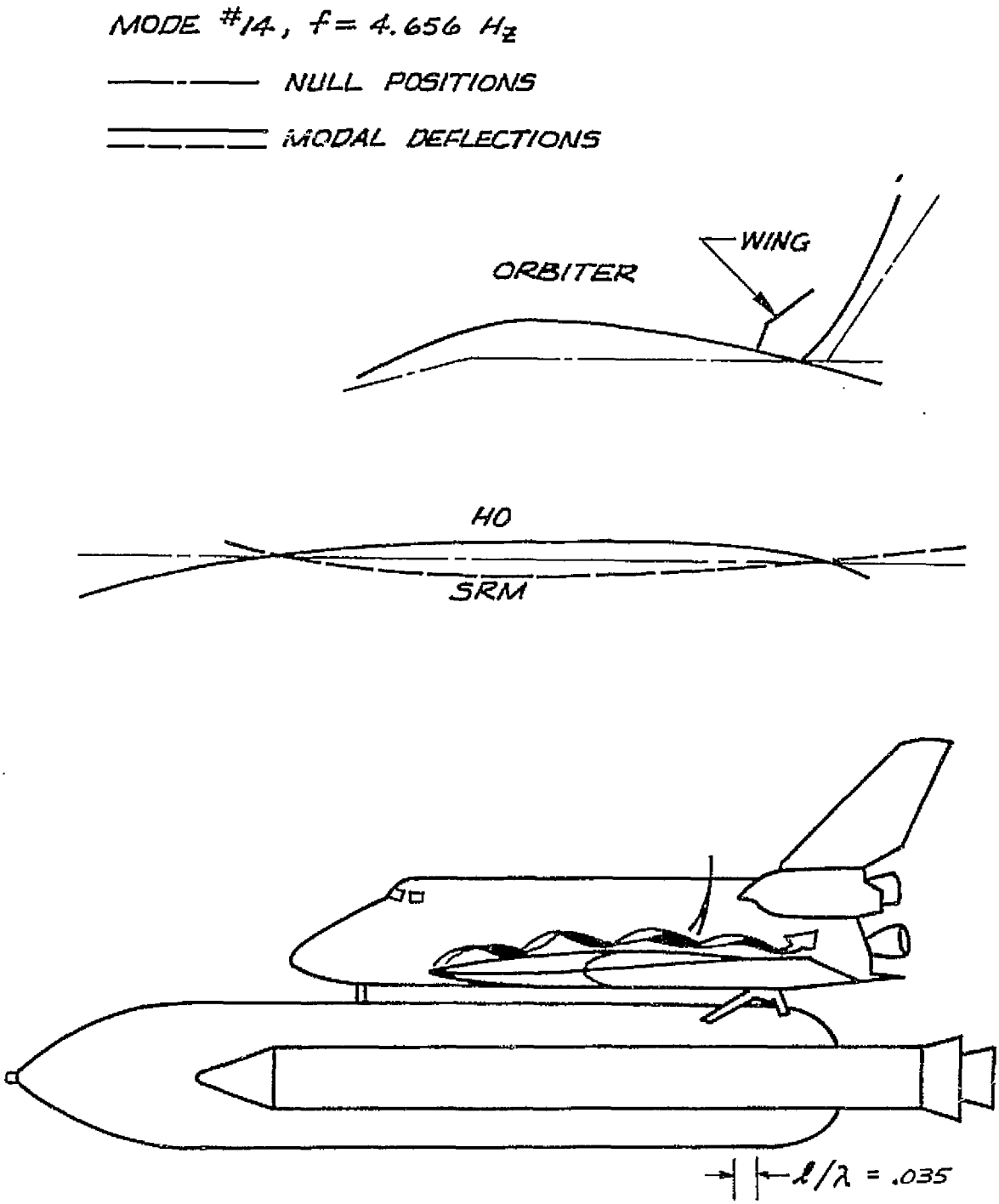

Figure 33 Sketch of Mode No. 14, f = 4.656 Hz

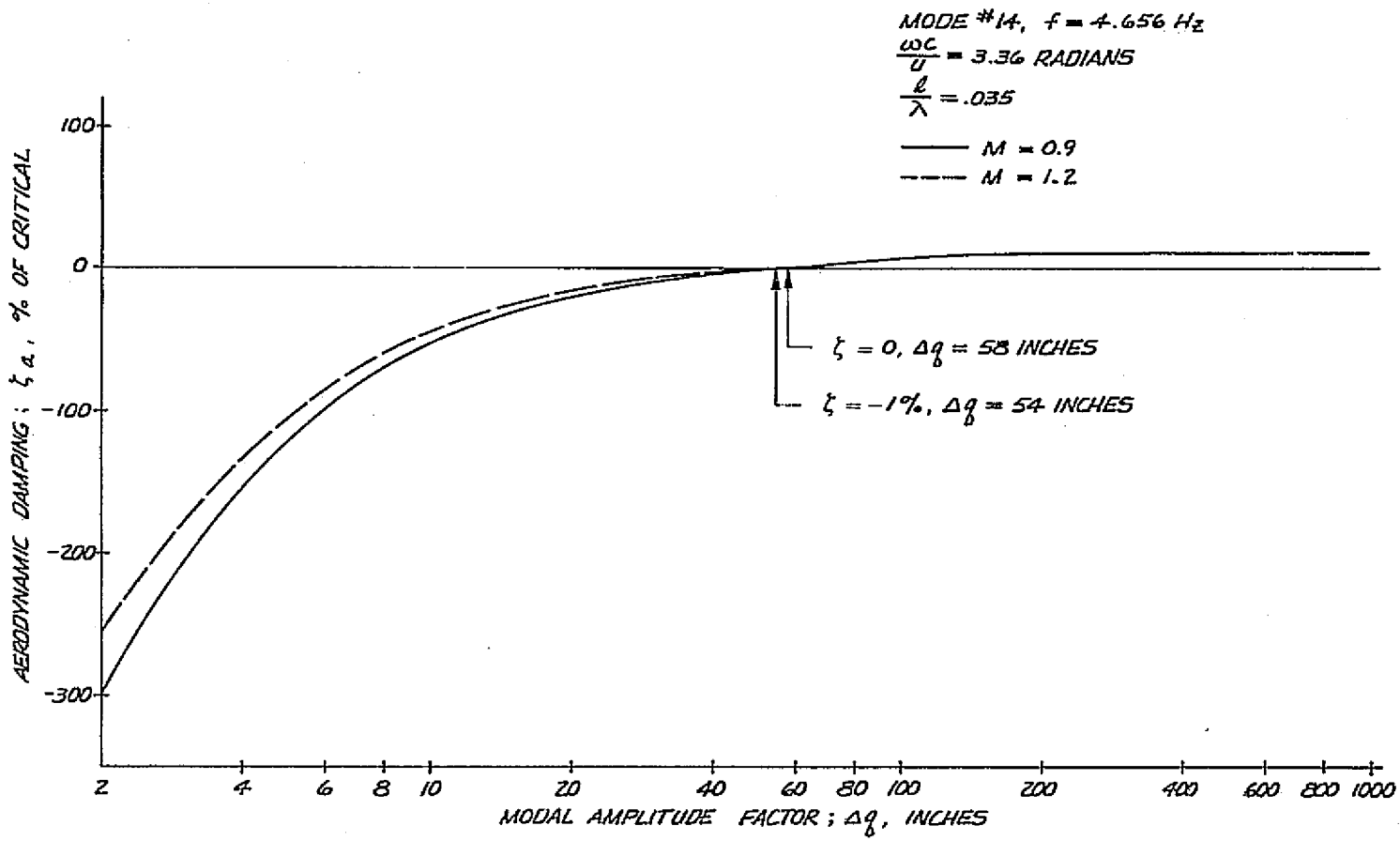

Figure 34 Effect of Orbiter Wing Shock Jump on the Aerodynamic Damping of the Launch Configuration Mode No. 14

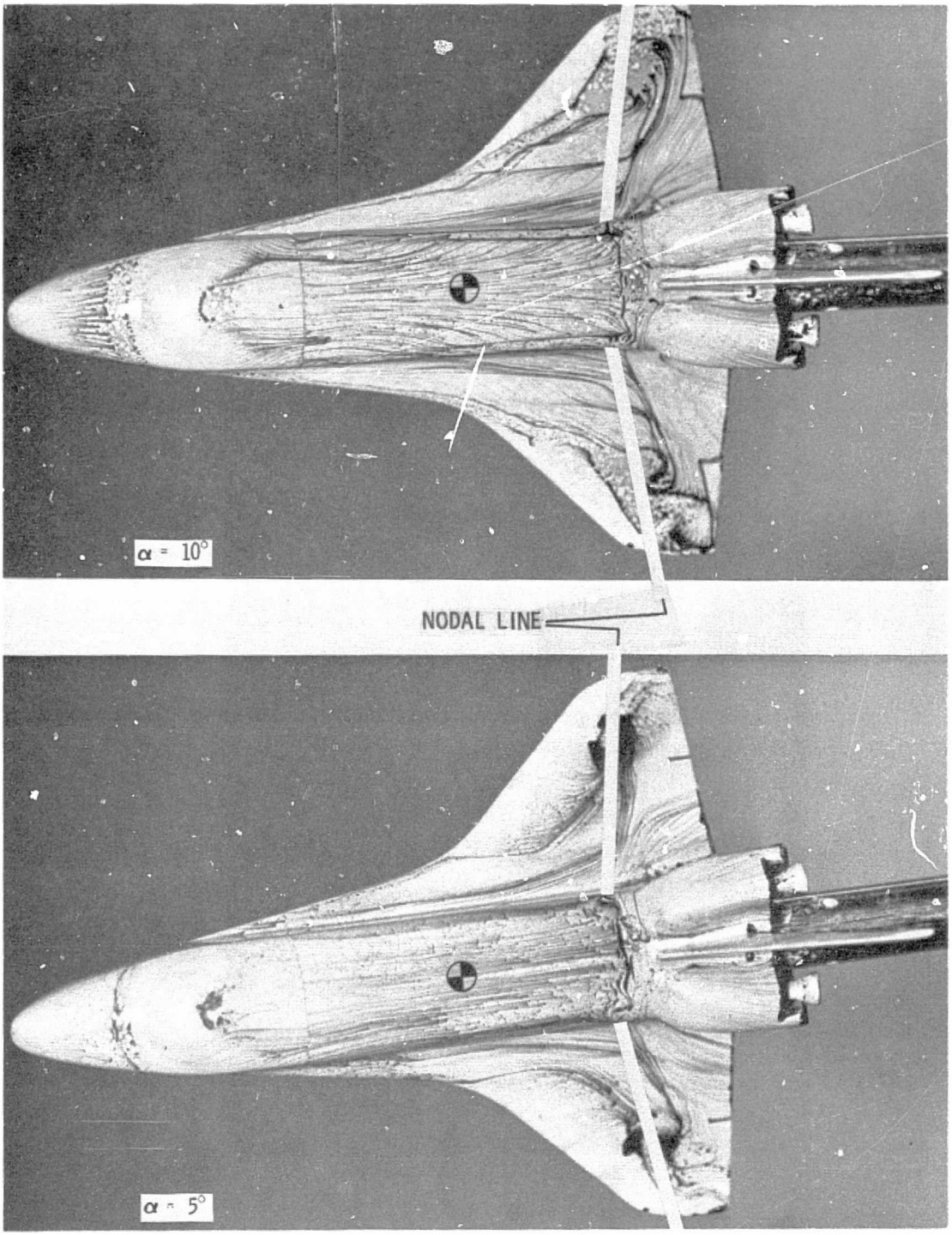

Figure 35 Correlation of Wing Torsional Mode Mode Line with Orbiter Wing Flow Patterns, M = 1.25

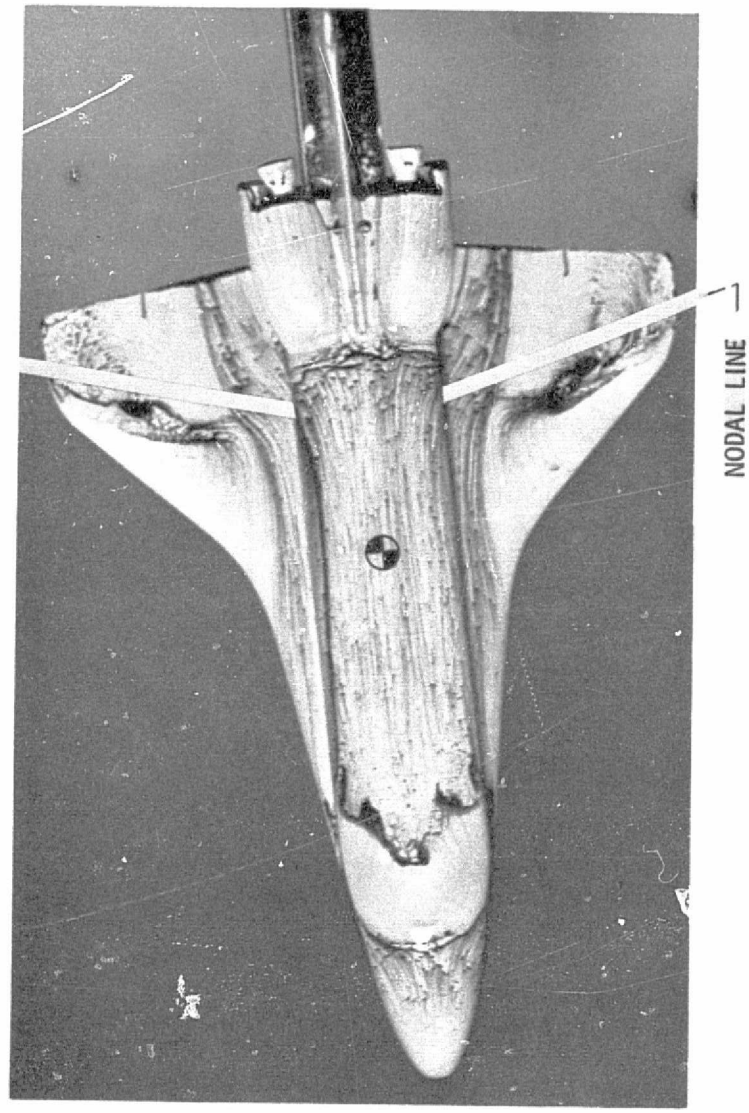

Figure 36 Correlation of Wing Torsional Mode Node Line with Orbiter Wing Flow Patterns, M = 0.9, α = 0

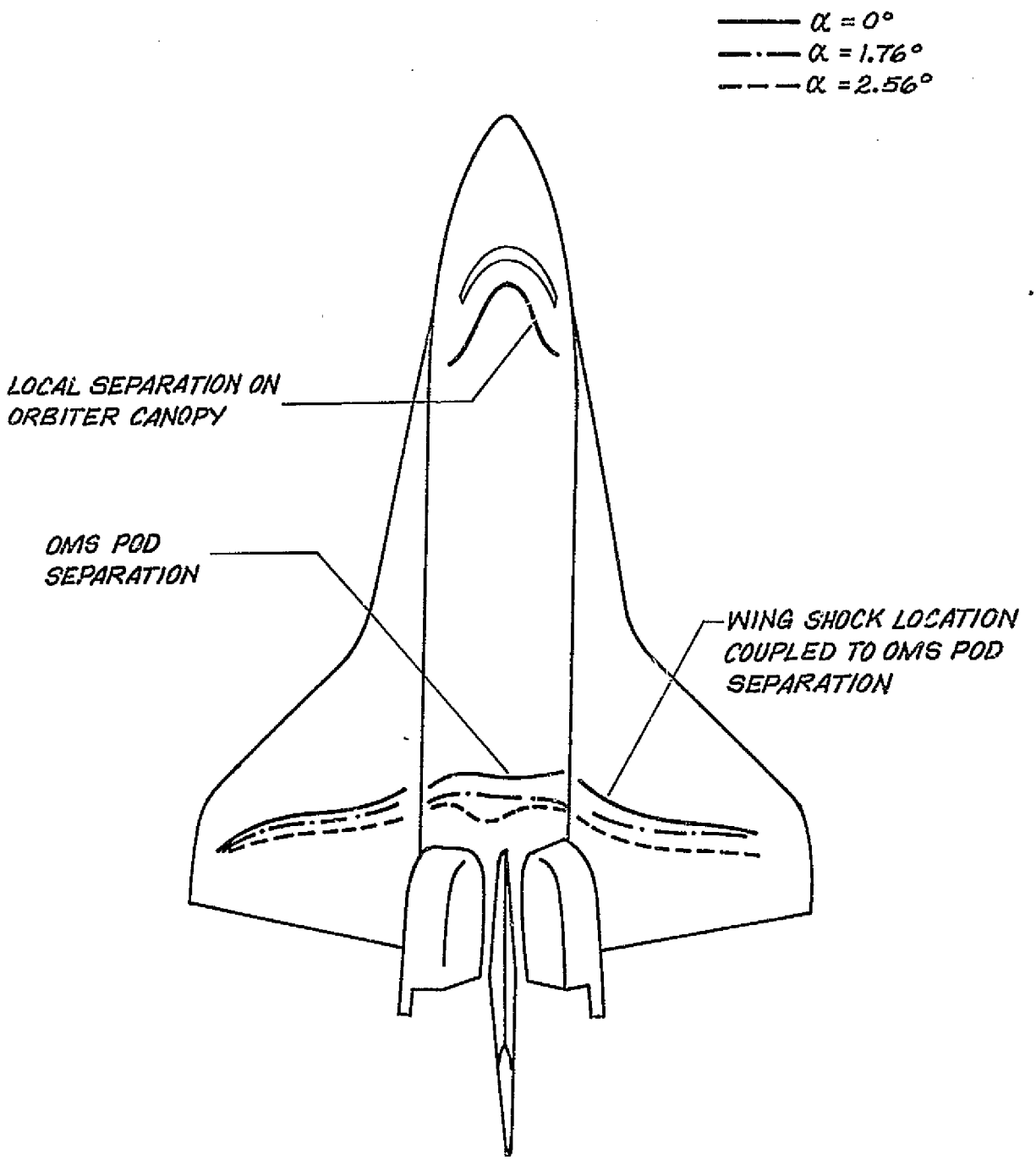

Figure 37 Effect of Angle of Attack on OMS Pod Separation and Wing Shock Locations at M = 1.2

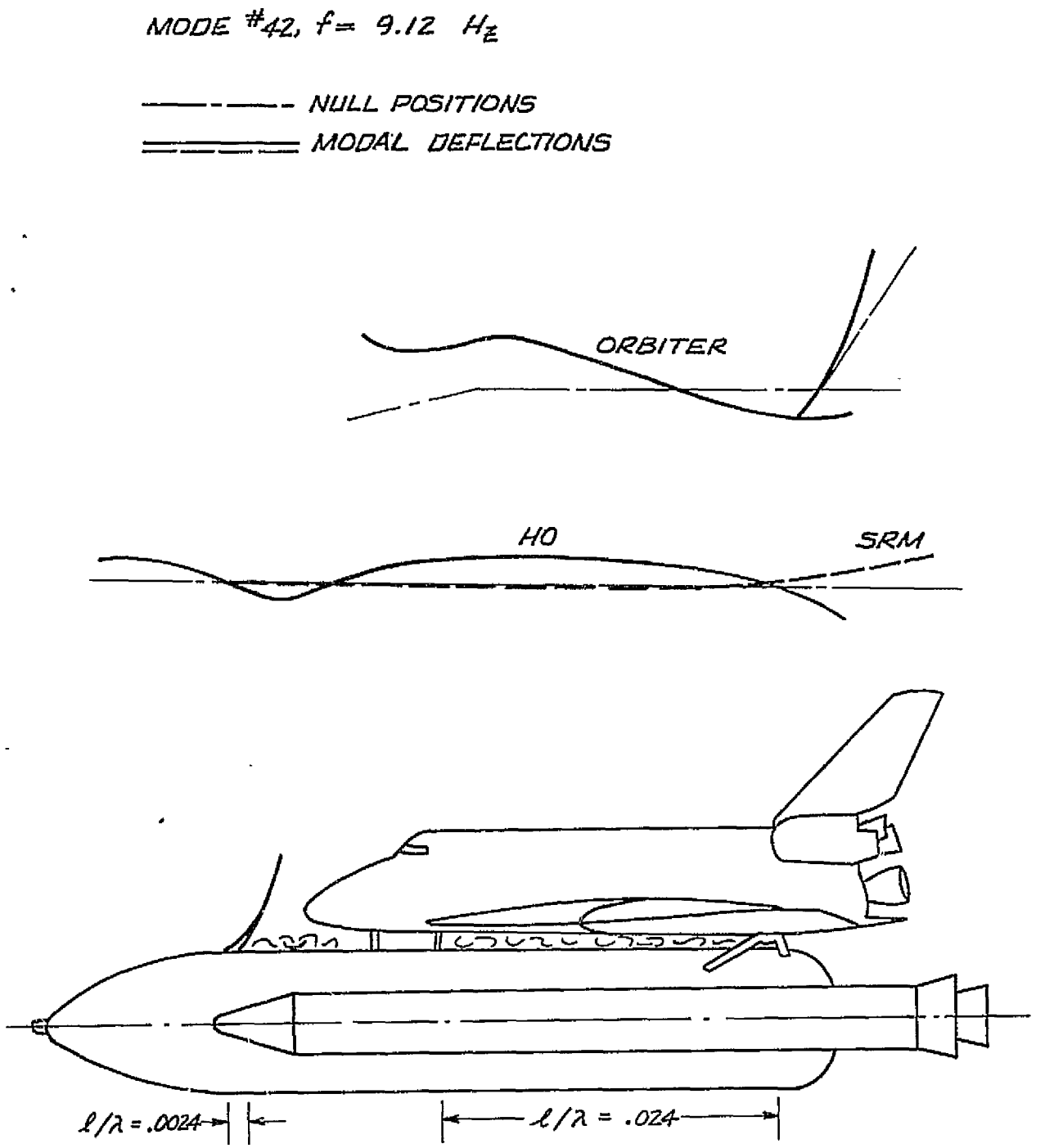

Figure 38 Sketch of Mode No. 42, f = 9.120 Hz

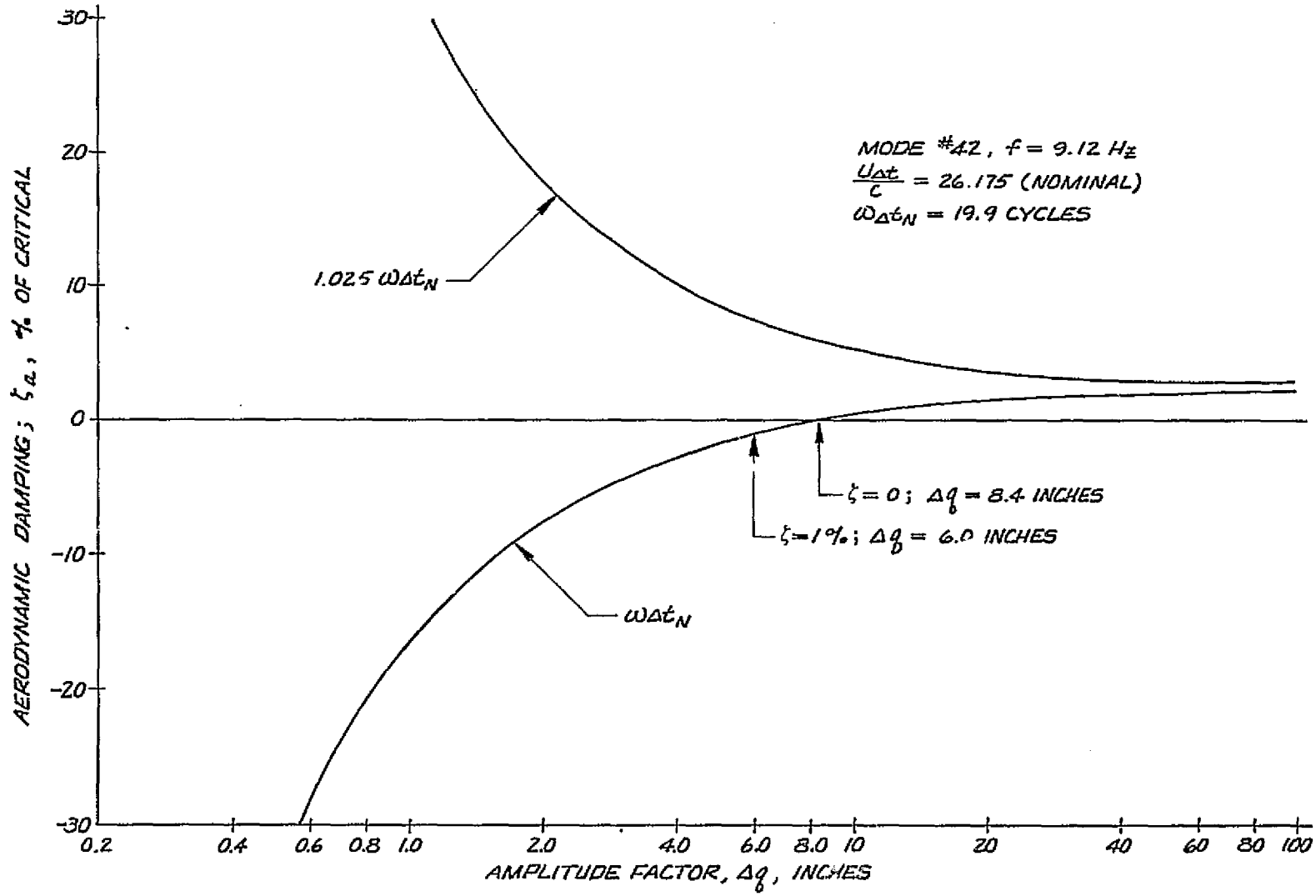

Figure 39 Effect of Inlet Flow on the Aerodynamic Damping of the Launch Configuration at M = 1.2, α = 2.2°

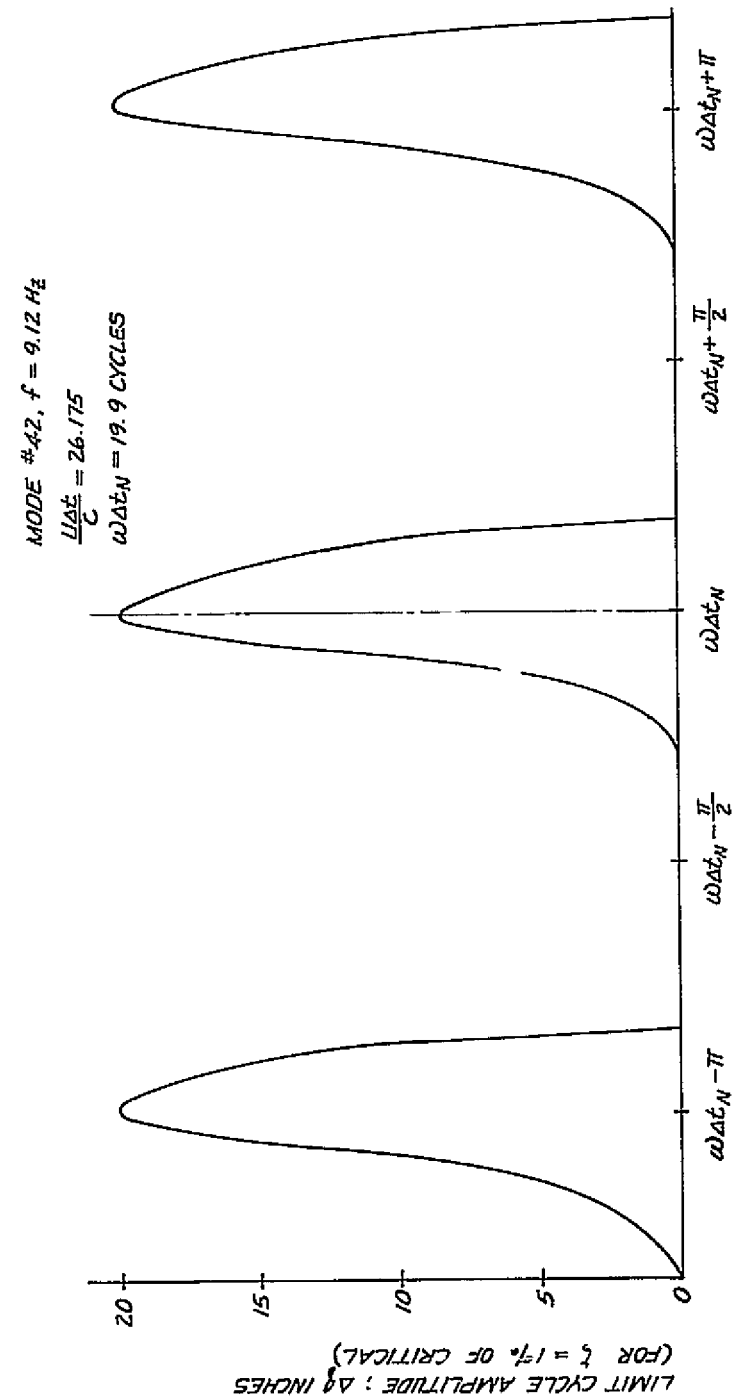

Figure 40 Effect of Phase Angle on Limit Cycle Amplitude for Inlet Flow, M = 1.2, α = 2.2°

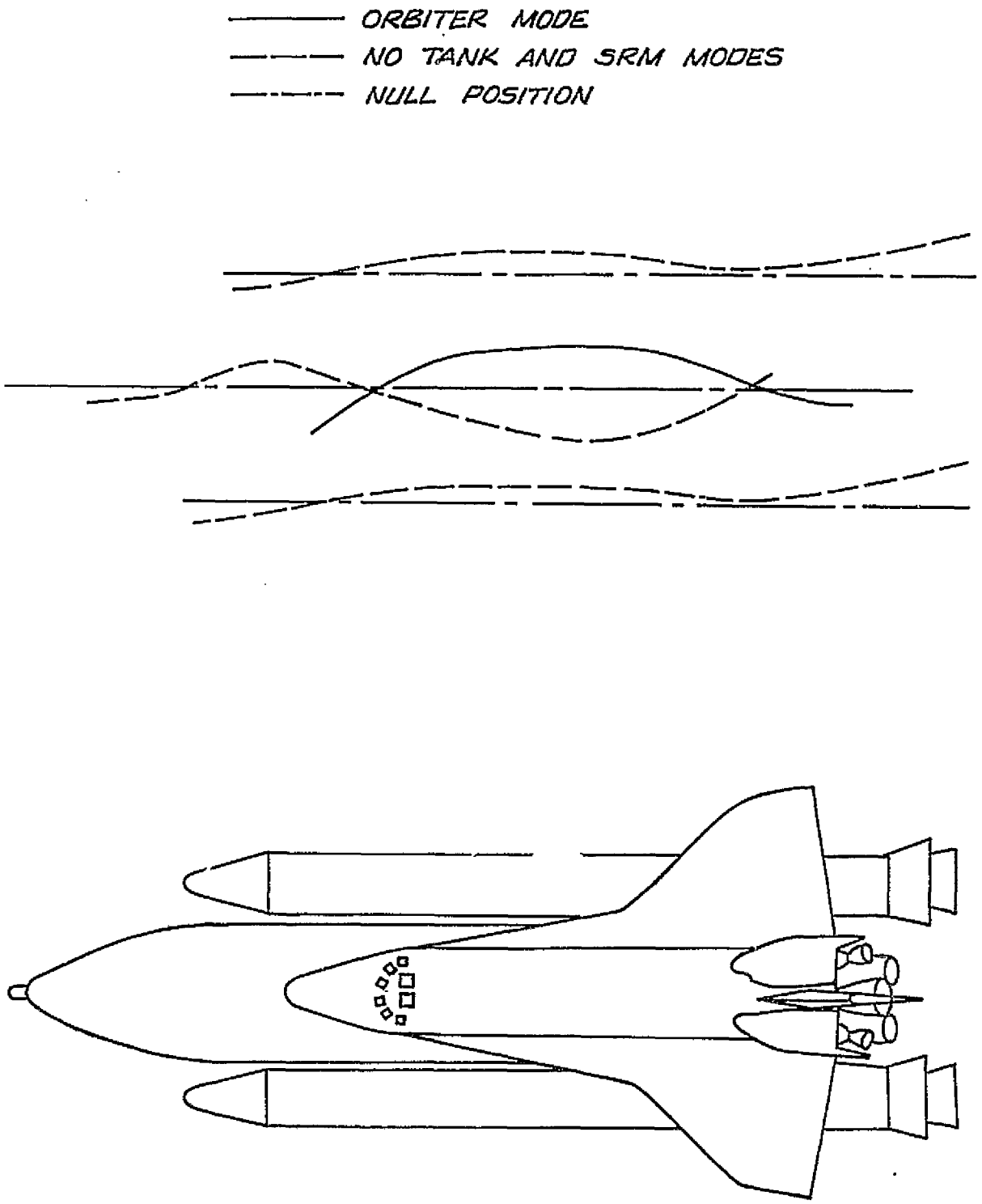

Figure 41 Sketch of Antisymmetric Mode No. 40, f = 8.43 Hz

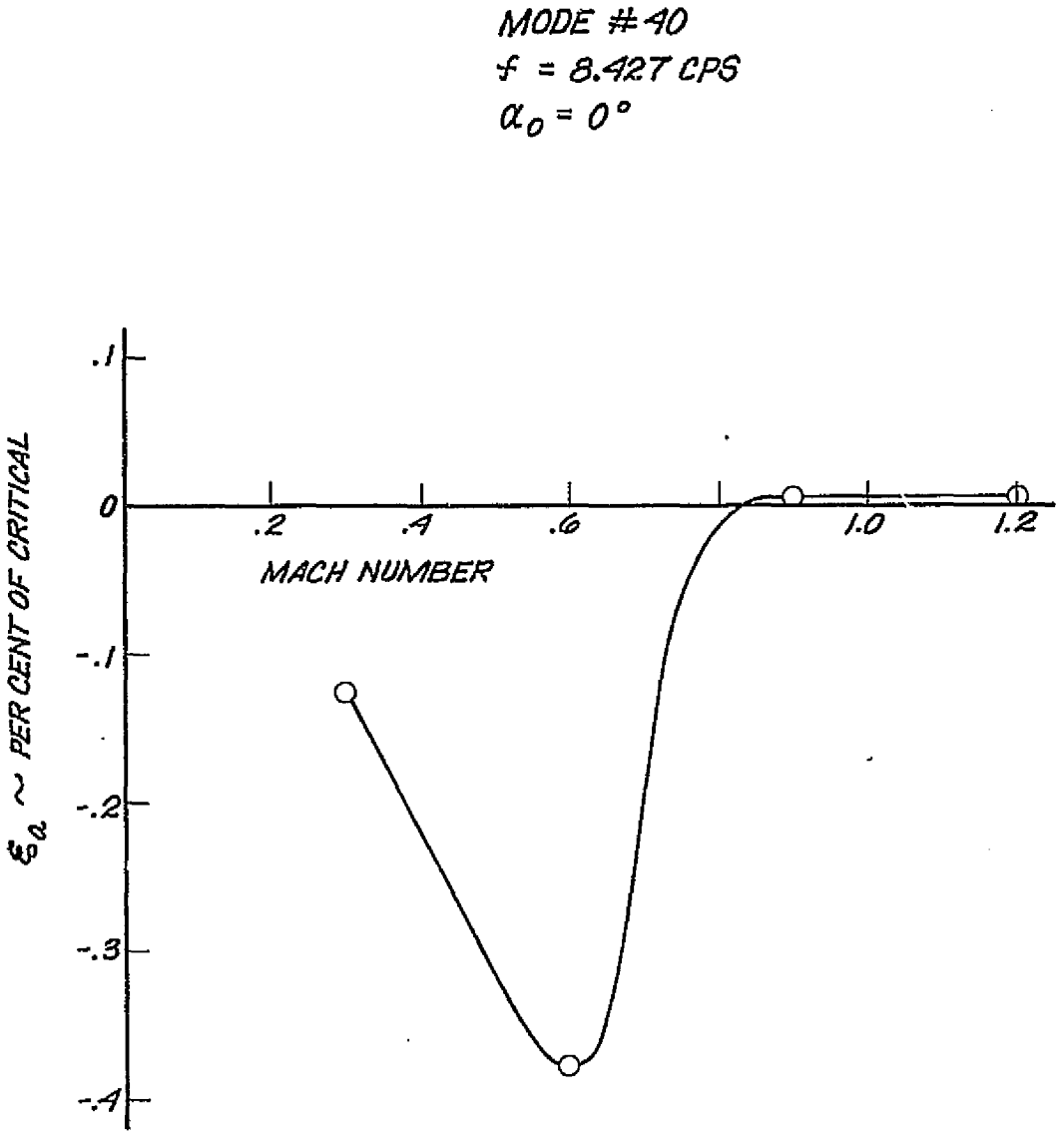

Figure 42 Effect of HO Tank Bulbous Base on Aerodynamic Damping of the Launch Configuration Mode No. 40